TR/14/88 December 1988

FESTER - An elasto-viscoplastic finite-element program for geotechnical applications.

M. B. Reed and D. A. Lavender

Technical report and user manual.

FESTER - AN ELASTO-VISCOPLATIC FINITE ELMENT PROGRAM FOR GEOTECHNICAL APPLICATIONS: TECHNICAL REPORT AND USER MANUAL

M. B. REED

D. A. LAVENDER

work on this project was sponsored by the Science and Engineering Research Council and British Coal.

z163185x

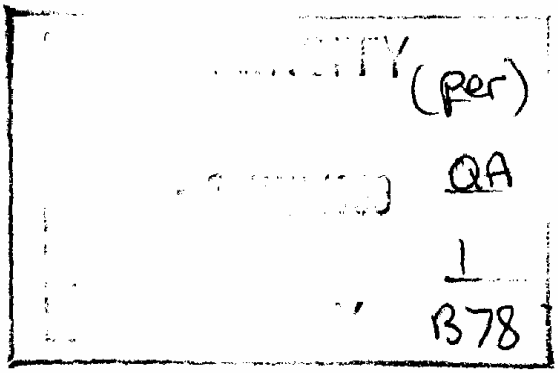

CONTENTS

SUMMARY:

The aim of the project was to produce a numerical model of the stresses and displacements which develop in a pre-stressed rock mass when a tunnel of arbitrary profile is excavated, assuming plane strain conditions. The resulting program, christened FESTER, is based on a two-dimensional elasto-viscoplastic analysis, using an implicit timestepping algorithm. Eight-noded isoparametric quadrilateral finite elements are used, together with elastic joint elements to allow relative slip between different rock strata, and infinite elements to represent the continuing rock mass at the mesh boundary. The program contains a number of features of particular relevance to rock mechanics applications, namely:

- use of a Hoek-Brown yield criterion as an alternative to the usual Mohr-Coulomb model;
- modelling of rock brittleness, and a low tensile strength;
- modelling of laminated rock, with anisotropic properties and allowing frictional sliding along a plane of weakness;
- a realistic loading-by-excavation algorithm;
- a simple variable-dilation nonassociated plastic flow rule.

In addition, a powerful pre- and postprocessor package has been developed, which runs on an IBM PC using Halo graphics. This allows mesh refinement (with automatic handling of boundary conditions, loads, etc.) and display of deformed meshes and principal stress plots. FESTER itself is written in Fortran 77, and is extremely portable between mainframes.

CHAPTER 1: OVERVIEW

1.1 Introduction

This report describes the Fortran 77 computer program **FESTER** (Finite Element Simulation of Tunnels Excavated in Rock), which has been developed on an S.E.R.C./British Coal co-funded research project. **FESTER** is intended to model the plane strain deformations and stresses in the rock mass surrounding an underground opening. It uses a nonlinear finite element analysis in two dimensions; the rock behaviour is modelled by the theory of elasto-viscoplaeticity, so that the progress of the deformation is followed over a nonphysical timescale.

In this chapter the various features of **FESTER** will be summarized, and in subsequent chapters the theory underlying the program will be explained. The separate pre-processor package is also described, and an appendix contains a user manual.

The program is based on a very general finite element package for linear elastic analyses; upon this foundation the nonlinear elasto-viscoplastic algorithm for plane strain analyses has been constructed. These two levels will now be described.

1.2 Elastic analyses

The linear elastic finite element package upon which **FESTER** is based, is **FINEPACK,** developed at the Department of Civil Engineering, University College Swansea (Naylor 1977). The basic theory, notation and program structure are set out in Hinton & Owen (1977). Basically, the material continuum is discretized by a mesh of finite elements, and for each element an element stiffness matrix is calculated, which relates nodal loads to nodal displacements. These matrices are then assembled into a global stiffness matrix K. Loads applied to the continuum are represented by a nodal load vector f, and the matrix equation

$$Ku = f \tag{1.2.1}$$

is solved, with appropriate boundary conditions, for the nodal displacements u. From these displacements, the strains and stresses at the Gaussian integration points of the elements may be calculated. The theory is summarized in section 2.1.

FINEPACK is written for analyses in one, two or three dimensions, and a wide range of element types are available, from the two-noded linear bar element to the twenty-noded parabolic brick element. In two dimensions there are linear and quadratic, triangular and quadrilateral elements. To this range has been added a five-noded mapped infinite element, which is

derived from the eight-noded quadrilateral element by letting one side be located at infinity. This is particularly useful in analysing deep-level excavations, where the rock mass is treated as of infinite extent. See section 2.2.

Loading may be by means of point loads at the nodes, distributed pressures across an element side/face, and body forces acting throughout the volume of an element. The latter two types of distributed load are converted into equivalent nodal loads by the program, for summing into the nodal load vector f. The type of loading occurring in underground excavations is slightly more complicated, however. Here, the continuum is in a state of equilibrium prior to excavation with the loading dictated by the in situ stress field. Deformation then occurs when these loads are removed around the wall of the opening by the process of excavation. For linear elastic analyses identical results will be obtained by simply applying the body forces from zero load and zero stress, or 'turning on the gravity'. This is not the case in nonlinear analyses, and the method of excavation loading has therefore been incorporated in **FESTER;** see section 2.3.

In linear elastic analyses the global stiffness matrix K will be symmetric, and advantage is taken of this in the subroutine to solve (1.2.1). The frontal method of solution is used, in which the matrix K is not fully assembled, but the assembly and Gaussian elimination processes are interleaved - this saves considerably on the core storage required. Solution techniques are discussed in section 4.3.

The general nature of **FINEPACK** has been preserved as far as possible in writing **FESTER.** However, **FESTER** has been designed only for two-dimensional plane strain analyses (instead of the plane strain, plane stress, axisymmetric and three-dimensional analyses possible with **FINEPACK)**, and it is intended that the mesh be constructed of eight-noded quadrilateral elements and the related infinite elements. **FESTER** may be extended to three-dimensional analyses in a subsequent project. Integration over each element is performed by a second-order Gauss rule, involving four Gauss integration points. It is at these Gauss points that the element stresses are evaluated once (1.2.1) has been solved for the nodal displacements.

FINEPACK assumed isotropic linear elasticity, defined in terms of a Young's modulus E and Poisson's ratio v. This has been generalized to orthotropic elasticity, with two sets of elastic parameters applying in orthogonal directions; see section 3.4. This orthotropy is a common feature of stratified, sedimentary rocks.

Throughout this text, the 'compression positive' sign convention for

Stresses and strains will be assumed.

1. 3 Viscoplastic analyses

The viscoplasticity theory used in **FESTER** is detailed in Owen & Hinton (1980), chapter 8; the programming notation of this text is consistent with that of **FINEPACK.** The theory is summarized in section 3.1. Once the Gauss-point stresses have been found from an elastic analysis, they are tested against a yield criterion $F(\sigma) > 0$ to determine if plastic yield has occurred. Where this is the case, an additional plastic strain increment is present, of a magnitude proportional to the extent by which the yield surface $F(\sigma) = 0$ has been exceeded, and in a direction determined by a plastic flow rule defined in terms of a stress function $Q(\sigma)$ known as the plastic potential. The essential equation may thus be written

$$\dot{\varepsilon}_P = \gamma < F(\sigma) > \frac{\partial Q}{\partial \sigma} \qquad (1.3.1)$$

where $< F > = F$ if $F > 0$, and is zero otherwise. γ is a fluidity parameter controlling the rate of deformation.

By discretizing (1.3.1) in time, an incremental stiffness equation

$$\hat{K}^{(n)} \Delta u^{(n)} = \Delta g^{(n)} \qquad (1.3.2)$$

is obtained, to be solved for the displacement increments over the time interval from t_n to $t_n + \Delta t_n$. The algorithm is given in section 3.1, but two classes of algorithm may be distinguished depending on the form of discretization employed. Writing

$$\Delta\varepsilon_P^{(n)} = \Delta t_n \left[(1-\theta)\, \dot{\varepsilon}_P^{(n)} + \theta \dot{\varepsilon}_P^{(n+1)}\right], \qquad (1.3.3)$$

taking the discretization parameter $\theta=0$ results in an explicit algorithm, whereas $0 < \theta \leq 1$ produces an implicit algorithm. The effect of this on (1.3.2) is to make $\hat{K}^{(n)} \equiv K$ in the explicit case, i.e. at each timestep the global stiffness matrix is unchanged from the initial elastic stiffness matrix. This makes the solution process at each timestep much faster than in the implicit algorithm; the disadvantage is that the timesteps must be kept small for stability, whereas the implicit algorithm is unconditionally stable if $\frac{1}{2} \leq \theta \leq 1$.

A further important characteristic of the method is determined by the choice of the yield function $F(\sigma)$ and plastic potential $Q(\sigma)$. Where these are identical, $F = Q$, the flow rule is termed associated, and in this case the stiffness matrix $\hat{K}^{(n)}$ will be symmetric. For non-associated flow $\hat{K}^{(n)}$ will be unsymmetric, unless of course the explicit algorithm is used.

Because of the greater work involved in solving (1.3.2) for unsymmetric $\hat{K}^{(n)}$, and the guaranteed well-conditioning of the problem when $\hat{K}^{(n)} = K$, the explicit algorithm has proved much more popular than the implicit in published work. An additional factor is the ease of programming: formation of $\hat{K}^{(n)}$ in the implicit case involves evaluating the Hessian matrix of second partial derivatives of $Q(\sigma)$. An important feature of **FESTER** is that it is possible to use the implicit as well as the explicit algorithm.

The standard yield criteria considered in plasticity texts are those of Von Mises, Drucker-Prager, Tresca and Mohr-Coulomb, of which the last-mentioned is the most appropriate for soils and rocks. **FESTER** uses the Mohr-Coulomb criterion, as well as a criterion due to Hoek and Brown which was derived from extensive triaxial testing of rock samples; see section 3.2.

An important feature of rock behaviour which needs to be modelled is brittleness, that is, a substantial loss of strength upon yield, due to micro-cracking. This is equivalent to a shrinkage of the yield surface $F(\sigma) = 0$ (see fig 1.3.1) in principal stress space, to a residual surface $F_R(\sigma) = 0$ which lies closer to the hydrostatic axis $\sigma_1 = \sigma_2 = \sigma_3$. Metals exhibit strain-hardening, i.e. a gradual expansion of the yield surface related to the amount of plastic strain, and by using a negative value of the hardening parameter a gradual strain-softening may be modelled in both elasto-plasticity and elasto-viscoplasticity theory. (At this point it is appropriate to point out the difference between the two theories. In elasto- plasticity, the stress state is not permitted to exceed the yield surface by more than an infinitesimal amount; the algorithm is an iterative one, with the stress states at yielded points being reduced down onto the yield surface at each iteration, which continues until an equilibrium is reached. In elasto-viscoplasticity, the yield surface may be exceeded temporarily, and the stress states are gradually brought down over time; the timestepping algorithm replaces the iterative process of elasto-plasticity.) The concept of brittleness is contrary to the asumptions of elasto-plasticity, since the sudden shrinkage of the yield surface at yield would leave the stress state significantly exceeding the residual surface; indeed, the elasto-plastic algorithm is highly unstable with strain-softening (see the review in Thomas 1984). For this reason elasto-viscoplastic theory is used in **FESTER.** It is then possible to model

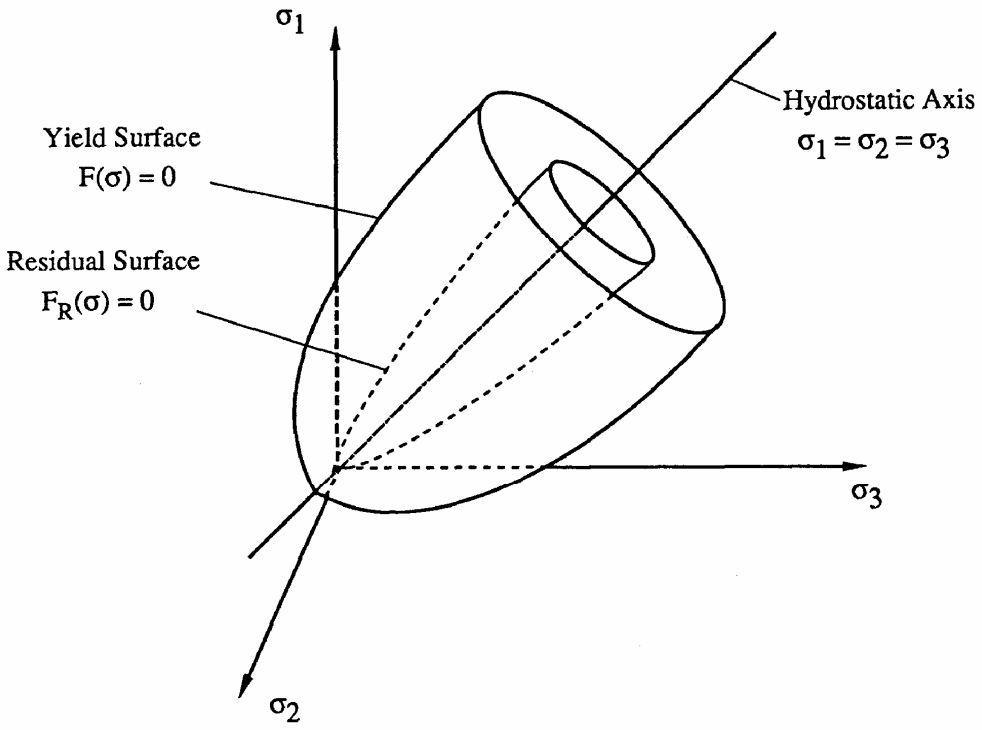

Figure 1.3.1

brittle rock by using $F(\sigma)$ in testing for initial yield, but $F_R(\sigma)$ in (1.3.1) thereafter. This also obviates the need for any difficult-to-determine strain-softening relationship. This aspect is discussed further in section 3.4.

The stress path followed during plastic flow, is dependent upon the choice of plastic potential $Q(\sigma)$ in the flow rule (1.3.1).

An associated flow rule, with $Q \equiv F$, is mathematically attractive, since in this case one can prove the existence of a unique solution to the general boundary value problem with ideal plasticity (Hill 1983). For strain-hardening materials this may also be the case with some non-associated flow rules (Korneev and Langer 1984, p.93). For strain-softening and brittle materials these theorems do not apply; the work done in plastic straining must be positive, however, which requires that $Q(\sigma)$ is a convex surface with the flow vector $\frac{\partial Q}{\partial \sigma}$ the outward normal from the surface at all points, that is $\sigma^T \frac{\partial Q}{\partial \sigma} > 0$ (Preévost and Hoëg 1975).

It has been observed that for geotechnical materials using the Mohr-Coulomb yield criterion, the associated flow rule produces results which greatly overestimate the displacements observed in practice. For this reason a plastic potential of Mohr-Coulomb type has been proposed (Zienkiewicz and Pande 1977) in which the angle of internal friction φ is replaced by an angle of dilation ψ, $0 \le \psi \le \varphi$. At one extreme, $\psi = \varphi$ gives the associated flow rule; at the other, $\psi = 0$ means that the flow vectors lie in the octahedral plane $\sigma_1 + \sigma_2 + \sigma_3 = 0$, so that there is zero plastic dilation. However, this flow rule suffers from the same drawbacks as the Mohr-Coulomb yield function, namely the difficulty in finding partial derivatives, and the presence of sharp corners on the surface which must be smoothed out in some fairly arbitrary way. Moreover, the flow rule tends to direct the stress state towards these corners in problems with axial symmetry (Sloan and Booker 1986, Reed 1986b). **FESTER** avoids these problems by using a simple non-associated flow rule of Drucker-Prager type; full details are given in section 3.3.

A further important aspect of rock behaviour which is modelled in **FESTER** is the existence of a plane of weakness. This is modelled in two ways: (i) orthotropic elastic parameters, as mentioned above; (ii) separate yield and no-tension criteria. Stresses are resolved parallel and normal to the plane of weakness, and a frictional yield criterion is used to limit the shear in this plane. Tensile stresses normal to the plane are also eliminated if they occur. The resultant plastic strain increments are added on to those arising in the conventional viscoplastic analysis. The method, described in section 3.5, is based on the multilaminate rock model of Zienkiewicz and Pande (1977).

Chapter 4 discusses some special techniques involved in the implicit algorithm, for the accurate formation of the stiffness matrices and solution of the matrix equation. In this algorithm the effect of large displacements can be taken into account (although the theory is still based on small strains).

Some numerical results are presented in Chapter 5.

CHAPTER 2: ELASTICITY

2. 1 Basic theory

The use of the finite element method for linear elasticity problems has been well-described in a number of texts (e.g. Zienkiewicz 1977, Hinton and Owen 1977, Greenough and Robinson 1981), but will be summarized here for completeness. Attention will concentrate on plane strain analyses; that is, situations in which there is no movement in the out-of-plane direction. This is a reasonable assumption in the case of a long tunnel, but it is clearly not valid close to the head of the tunnel, where a full three-dimensional analysis would be needed. In linear elastic analyses of plane strain problems, the out-of-plane stress remains constant during the deformation, and is usually omitted from the calculations; it does need to be considered in plasticity theory, however, and will therefore be introduced at the outset, as the last component of the stress vector.

The state of stress at any point in the material continuum is expressed by the stress vector

$$\sigma = (\sigma_x \ \sigma_y \ \tau_{xy} \ \sigma_z)^T$$

where τ_{XY} is the shear stress in the xy-plane, and $\sigma_x, \sigma_y, \sigma_z$ are the normal stresses (the z-direction being the out-of-plane direction; there are no shear stresses in the xz- and yz-planes). The corresponding strain vector is

$$\varepsilon = (\varepsilon_x \ \varepsilon_y \ \gamma_{xy} \ \varepsilon_z)^T$$

and the stress and strain are linked by the elastic constitutive D-matrix:

$$\sigma = D\varepsilon \tag{2.1.1}$$

which in plane strain is written in terms of the Young's modulus E and Poisson's ratio ν as

$$D = \frac{E}{(1+\nu)\ (1-2\nu)} \begin{bmatrix} 1-\nu & \nu & 0 & \nu \\ \nu & 1-\nu & 0 & \nu \\ 0 & 0 & \frac{1}{2}(1-2\nu) & 0 \\ \nu & \nu & 0 & 1-\nu \end{bmatrix} \tag{2.1.2}$$

Since there is no displacement in the z-direction, the displacement vector is simply

$$u = (u \ v)^T$$

with u and v the displacements in the x- and y-directions respectively. The elastic strains caused by a set of displacements u are

$$\varepsilon_x = \frac{\partial u}{\partial x}\ ,\ \varepsilon_y = \frac{\partial v}{\partial y}\ ,\ \gamma_{xy} = \frac{\partial u}{\partial y} + \frac{\partial v}{\partial x} \qquad (2.1.3)$$

where second-order terms are ignored, i.e. assuming small strains.

If an elastic body is subjected to a set of boundary tractions t and body forces b, then by the Principle of Virtual Work

$$\int_\Omega \delta\varepsilon^T \sigma d\Omega - \int_\Omega \delta u^T b d\Omega - \int_\Gamma \delta u^T t d\Gamma = 0 \qquad (2.1.4)$$

where δu, $\delta\varepsilon$ are the virtual displacements and strains, Ω represents the body and Γ its loaded boundary.

In the finite element method, the displacements at any point (x,y) are approximated as a linear combination of the nodal displacements for the element in which that point lies, i.e.

$$u = Nd^{(e)} \qquad (2.1.5)$$

where

$$N = \begin{bmatrix} N_1 & N_2 & \dots & N_n \\ N_1 & N_2 & \dots & N_n \end{bmatrix}$$

is the matrix of shape or basis functions corresponding to nodes 1,2,..,n of the element, evaluated at (x,y), and

$$d^{(e)} = (u_1\ v_1\ u_2\ v_2\ \dots\ u_n\ v_n)^T$$

is the vector of nodal displacements. Combining (2.1.3) and (2.1.5) gives a strain-displacement relationship

$$\varepsilon = Bd^{(e)}\ . \qquad (2.1.6)$$

Using (2.1.5) and (2.1.6) in the virtual work principle (2.1.4), which must hold for an arbitrary set of displacements δu, gives

$$\int_\Omega B^T\sigma\ d\Omega - \int_\Omega N^T b\ d\Omega - \int_\Gamma N^T t\ d\Gamma = 0 \qquad (2.1.7)$$

Applying (2.1.1) and (2.1.6) gives the global stiffness equation

$$Kd = f \qquad (2.1.8)$$

where the global stiffness matrix K is assembled from element stiffness matrices

$$K^{(e)} = \int_{\Omega e} B^T DB d\Omega\ ,$$

the consistent load vector is

$$f = \int_{\Omega} N^T b \; d\Omega + \int_{\Gamma} N^T t \; d\Gamma \;,$$

and **d** is the global vector of nodal displacements.

2. 2 Element types

For two-dimensional analyses, **FINEPACK** has provision for the following types of elements to be used in the mesh: three- and six-noded triangles, and four-, six- and eight-noded quadrilaterals. Linear elements (three-noded triangles and four-noded quadrilaterals) can only represent stress and strain fields as constant over each individual element. Quadratic triangular elements suffer the disadvantage that the Gauss integration points lie on the element edges, where the stress field will be discontinuous, and are thus inappropriate as locations at which to keep track of the stresses in the viscoplastic algorithm (as are the nodes, for the same reason). We focus attention therefore on the well-known isoparametric eight-noded quadrilateral element, which is very popular in geotechnical applications. The element is shown in fig.2.2.1, in a general form in the xy-plane, and in canonical form in terms of the local coordinates ξ,η.

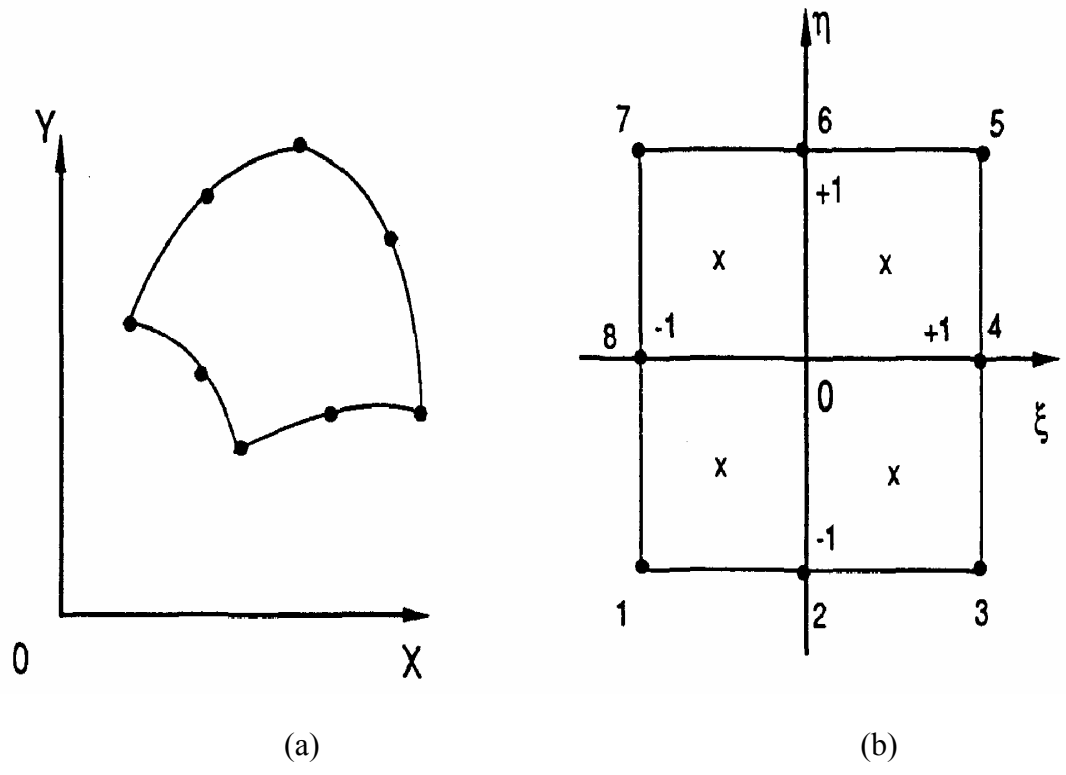

(a) (b)

Figure 2.2.1

The shape functions associated with the element are:
for corner nodes,

$$N_1\ (\xi, \eta) = \tfrac{1}{4}(1-\xi)\ (1-\eta)(-\xi-\eta-1)$$

$$N_3\ (\xi, \eta) = \tfrac{1}{4}(1+\xi)\ (1-\eta)(\xi-\eta-1)$$

$$N_5\ (\xi, \eta) = \tfrac{1}{4}(1+\xi)\ (1+\eta)(\xi+\eta-1)$$

$$N_7\ (\xi, \eta) = \tfrac{1}{4}(1-\xi)\ (1+\eta)(-\xi+\eta-1) \qquad (2.2.1)$$

and for midside nodes,

$$N_2\ (\xi, \eta) = \tfrac{1}{2}(1-\xi^2)\ (1-\eta)$$

$$N_4\ (\xi, \eta) = \tfrac{1}{2}(1+\xi)\ (1-\eta^2)$$

$$N_6\ (\xi, \eta) = \tfrac{1}{2}(1+\xi^2)\ (1+\eta)$$

$$N_8\ (\xi, \eta) = \tfrac{1}{2}(1-\xi)\ (1-\eta^2)$$

The x and y coordinates as well as the displacements at any point in the element can be expressed as a linear combination of the nodal values:

$$\varphi(x,y) \sum_{i=1}^{8} N_i\ (\xi,\eta)\ \varphi_i\ . \qquad (2.2.2)$$

A further advantage of this element over the linear elements is its ability to model curved boundaries, which will be useful in tunneling problems.

A 2 × 2 Gauss integration rule is used to approximate integrals over the element:

$$\int_{-1}^{1}\int_{-1}^{1} f(\xi,\eta)d\xi d\eta = \sum_{j=1}^{4} w_j f(\xi_j, n_j) \qquad (2.2.3)$$

where the weights $w_1 = w_2 = w_3 = w_4 = 1.0$, and the Gauss integration points are $\xi_j, n_j = \pm 1/\sqrt{3}$ (marked by crosses in fig 2.2.1b). It is at these integration points that the stresses will be evaluated.

Infinite element

In geotechnical applications it is common to need to model a material continuum which extends to infinity in one or more directions. For this purpose a family of mapped infinite elements has been proposed (Zienkiewicz, Emson and Bettess 1983), and shown to improve the accuracy of the solution when compared to the conventional technique of extending the mesh of finite elements until the boundary ceases to influence the results significantly. It has been successfully employed in a number of applications; the particular member of this family to be described has

been used in conjunction with eight-noded quadrilateral elements in plane strain elasto-plasticity analyses by Marques and Owen (1984). It is a five-noded element, derived from the eight-noded quadrilateral by extending the side at $\eta = +1$ to infinity; it is shown in general and canonical form in fig 2.2.2.

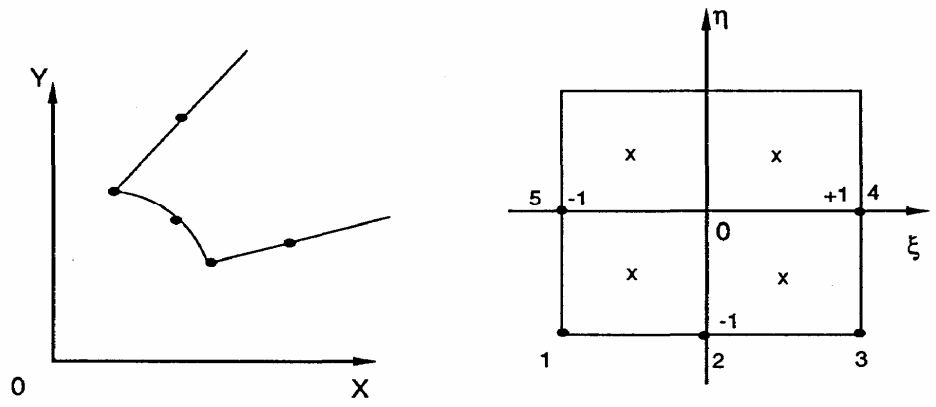

(a) (b)

Figure 2.2.2

The mapping from x,y to ξ,η coordinates is defined by a set of mapping functions $M_1,(\xi,\eta,),...,M_s\ (\xi,n)$ which diverge to infinity as $n \rightarrow 1$. Interpolation of the field variable φ is still performed by the standard shape functions from (2.2.1) for the five nodes of the element - this is equivalent to assuming that φ decays to zero at the infinite boundary. Thus, field variables are interpolated by

$$\varphi(x,y) = \sum_{i=1}^{5} N_i(\xi,\eta)\varphi_i \qquad (2.2.4)$$

but the mapping functions are used in the integration process and location of the Gauss-point coordinates, for example

$$x = \sum_{i=1}^{5} M_i(\xi,n)x_i \qquad (2.2.5)$$

Thus the Jacobian matrix is formed using the mapping functions and their derivatives, but the B matrix is formed using the shape functions,

when the stiffness matrix of the element is formed by Gaussian integration of

$$K^{(e)} = \int_{-1}^{1}\int_{-1}^{1} B^T D B \ \det J \ d\xi d\eta \qquad (2.2.6)$$

The shape and mapping functions for the five-noded mapped infinite element are

Mapping function	Shape function
$M_1 = (1-\xi)(-1-\xi-\eta)/(1-\eta)$	$N_1 = \frac{1}{4}(1-\xi)\ (1-\eta)\ (-1-\xi-\eta)$
$M_2 = 2(1-\xi^2)/(1-\eta)$	$N_2 = \frac{1}{2}(1-\xi^2)\ (1-\eta)$
$M_3 = (1+\xi)\ (-1+\xi-\eta)/(1-\eta)$	$N_3 = \frac{1}{4}(1+\xi)(1-\eta)(-1+\xi-n)$
$M_4 = \frac{1}{2}(1+\eta)(1+\xi)/(1-\eta)$	$N_4 = \frac{1}{2}(1+\xi)\ (1-\eta^2)$ (2.2.7)
$M_5 = \frac{1}{2}(1+\eta)(1-\xi)/(1-\eta)$	$N_5 = \frac{1}{2}(1-\xi)\ (1-\eta^2).$

This element has been added to the repertoire of two-dimensional elements available in **FINEPACK**.

Joint element

In geomechanics applications it is often desirable to model interfaces between rock strata and imperfections such as faults. A finite element has been introduced into the FESTER package to model these very situations. The essential property of these features is an interface which allows the two sides to slide relatively easily past each other. The element described here is essentially the same as that proposed by Goodman et al. in 1968. However, the derivation of the stiffness matrix is taken from schäfer (1975). This formulation has been retained here because of its simplicity, and because the alternatives have their own drawbacks. A different formulation was proposed by Ghaboussi et al. (1973) who found that the original Goodman version could lead to ill-conditioning of the stiffness matrix. However, Pande and Sharma (1979) have done some numerical experiments which suggest that ill-conditioning is not a real problem with modern high accuracy computers. The Goodman joint has a zero thickness and it is difficult to prevent opposite faces of the joint interpenetrating. In an effort to overcome this and other problems, Desai et al. (1984) have proposed a thin layer element that has a definite thickness. However, this element posesses numerical properties that vary with its aspect ratio, and leaves the problem of having to choose a suitable thickness for the element for each application.

The treatment here will be restricted to a summary of the derivation of

the stiffness matrix for the element. More details and some of the matrices written out in full may be found in Goodman et al. (1968) and schäfer (1975). The element is illustrated in fig. 2.2.3. The two faces of the element are assumed to coincide. For the moment we assume that we know the normal and tangential displacements u_{in} and u_{it} at each node i and we write them in a vector $\mathbf{u} = (u_{1\,n},\ u_{1\,t},\ u_{2n},\ldots\ldots,u_{6t})^T$ We can now obtain a vector of relative displacements

$$\Delta\mathbf{u} = \mathbf{A}\ \mathbf{u} \tag{2.2.8}$$

where **A** is a 6×12 matrix given by

$$aij = \begin{cases} 1 \text{ if } i = j \\ -1 \text{ if } i = j+6, \\ 0 \text{ otherwise} \end{cases}$$

The (interpolated) relative displacement at any point along the element can
now be obtained from the usual 1 dimensional shape functions

$$\mathbf{r}(x,y)=\mathbf{N}(x,y)\,\Delta u \tag{2.2.9}$$

where N is a 2 × 6 matrix containing the shape functions for the point (x,y) and r is the vector (r_n, r_t) of the normal and tangential relative displacements. A simple stiffness matrix is now used to obtain the forces acting due to these displacements

$$\mathbf{p} = \mathbf{K}\ \mathbf{r} \tag{2.2.10}$$

where

$$\mathbf{K}=\begin{bmatrix} k_n & 0 \\ 0 & k_t \end{bmatrix}$$

where k_n and k_t are the normal and tangential stiffnesses for the joint. We now use the principle of virtual work. Suppose that **f** is a vector of nodal forces and that δu is a small change in **u**, then, setting the internal and external work done equal gives

$$\boldsymbol{\delta u}^T\mathbf{f} = \int_{\text{elements}} \boldsymbol{\delta u}^T\mathbf{A}^T\mathbf{N}^T\ \mathbf{K}\ \mathbf{N}\ \mathbf{A}\ \mathbf{u}\ ds$$

where is the distance along the element. Since $\boldsymbol{\delta u}^T$ is arbitrary and we arrive at the form

$$\mathbf{f} = \mathbf{K_e}\ \mathbf{u} \tag{2.2.11}$$

where $\mathbf{K_e}$ is the finite element stiffness matrix. The integration may be carried out in local coordinates by transforming from global coordinates in the usual way.

In practice the expression for the finite element stiffness matrix will contain an extra matrix which rotates the components of the nodal displacements to give the normal and tangential displacements. In general the angle of rotation is different for each pair of nodes, and must be worked out from the shape mapping from local to global coordinates. When numerical quadrature is used to evaluate the integral it is necessary to use a 3 point rule in this case to avoid a singular global stiffness matrix resulting.

2.3 Types of loading

FINEPACK has provision for the following types of loading in two dimensions:

(i) point loads applied at the nodes:

(ii) surface tractions applied along the edge of an element (their magnitude may vary linearly along the edge of a linear element, and parabolically along the edge of a higher-order element);

(iii) body forces acting over the volume of an element.

Forces of the latter two types are converted into equivalent nodal loads before being summed into the global consistent nodal load vector. The procedure may be found in Hinton and Owen (1977).

The deformations around underground openings typically occur by a process of unloading rather than loading; that is, the rock mass is in equilibrium under a compressive in situ stress field prior to excavation, and these stresses are removed around the wall of the tunnel by the excavation process. In nonlinear analyses it is important to follow this loading process rather than to start with zero stresses and then 'turn on the gravity'.

In situ stresses underground are normally described by means of a vertical stress σ_V (usually taken to be the cover load) and a lateral stress ratio K_o (usually in the range $\frac{1}{2} \leq K_o \leq 1$), so that the horizontal stress $\sigma_H = K_o \sigma_V$.

The nodal loads $\mathbf{f}_o$ consistent with a given in situ stress field $\boldsymbol{\sigma}_o$ are found by integrating over each element:

$$\mathbf{f}_o = \int_{\Omega_e} B^T \sigma_o \, d\Omega \, . \qquad (2.3.1)$$

In **FESTER** the in situ stresses are prescribed by σ_V (either a constant or a cover load, in which case the unit weight of soil and the depth of the origin below ground level are input) and K_0, and the stresses at the element Gauss points - including the out-of-plane stress - stored in an

array STRSG. The integration (2.3.1) is performed element-by-element and the nodal loads summed into the global nodal load vector. These loads and internal stresses, with zero displacements, constitute the initial equilibrium state. The deformations are caused by applying equal and opposite loads on the nodes around the tunnel wall, to represent the excavation process.

In nonlinear analyses the load should be added in increments, and provision is made for this in **FESTER,** each new increment being applied when there is no further significant plastic deformation from the current load.

As well as modelling the rock mass, it is possible to use linear elastic finite elements around the tunnel wall to model support mechanisms such as concrete lining or steel arches. (In the latter case, the plane strain elements will be only a rough approximation to what is essentially a three-dimensional structure). These elements are omitted from the initial stress integration process, as they do not contain in situ stresses. They are distinguished from linear elastic rock elements in **FESTER** by a special material type code - see section 3.6.

It is commonly suggested that the viscoplasticity matrix $\hat{D}$ be simplified to

$$\hat{D}^n = (D^{-1} + \theta \Delta t_n H^n)^{-1} \qquad (3.1.12)$$

but it has been found in using **FESTER** on problems with axial symmetry that this simplification can give rise to numerical errors when a Poisson's ratio v close to $\frac{1}{2}$ is used; this is because the matrix D is singular at $v = \frac{1}{2}$.

At time t_n the applied nodal loads $\mathbf{f}^n$ and internal stresses $\boldsymbol{\sigma}^n$ are in equilibrium through the equation

$$\int_\Omega B^T \boldsymbol{\sigma}^n \partial\Omega - \mathbf{f}^n = 0, \qquad (3.1.13)$$

which in incremental form is

$$\int_\Omega B^T \Delta\boldsymbol{\sigma}^n d\Omega - \Delta\mathbf{f}^n = 0 \qquad (3.1.14)$$

where $\Delta\mathbf{f}^n$, the change in applied load over the time interval $[t_n, t_{n+1},]$, is zero for all time steps except the first within each load increment. Using (3.1.10) to substitute for $\Delta\boldsymbol{\sigma}^n$, (3.1.14) leads to the global stiffness equation to be solved for the displacement increments:

$$\mathbf{K}^n \Delta\mathbf{d}^n = \Delta\mathbf{v}^n \qquad (3.1.15)$$

where the global stiffness matrix is

$$K^n = \int_\Omega B^T \hat{D}^n B \, d\Omega$$

and the right-hand-side vector is

$$\Delta v = \int_\Omega B^T \hat{D}^n \dot{\varepsilon}^n_{vp} \Delta t_n \, d\Omega + \Delta\mathbf{f}^n.$$

Unfortunately the resulting state of stress and deformation of the continuum will not exactly satisfy the equation of equilibrium (3.1.13), because the linearized approximation (3.1.14) is used, and approximations have been made in (3.1.5) and (3.1.6). The simplest way to compensate for this is to evaluate the residual force vector:

$$\boldsymbol{\psi}^{n+1} = \int B^T \boldsymbol{\sigma}^{n+1} d\Omega + \mathbf{f}^{n+1} \qquad (3.1.16)$$

and add this to the new applied force increment at the next step. This is used in FESTER; alternative approaches to the problem of equilibrium correction are assessed by Stricklin et al (1973).

In essence, the viscoplastic algorithm applied within each timestep is thus:

(i) use the current stress state $\boldsymbol{\sigma}^n$ to find $\dot{\varepsilon}_{vp}^n$ by (3.1.4), at each Gauss-point;

(ii) hence find $\hat{D}^n$, K^n and ΔV^n by (3.1.10) and (3.1.15);

(iii) solve (3.1.15) to find the new displacements

$$\mathbf{d}^{n+1} = \mathbf{d}^n + \Delta\mathbf{d}^n \qquad (3.1.17)$$

(iv) for each Gauss-point, update the stresses similarly using (3.1.9);

(v) calculate $\boldsymbol{\psi}^{n+1}$ by (3.1.16) to use in the next timestep.

Full details of the computational procedure, choice of timestep length, criterion for convergence, etc., are given in Owen and Hinton (1980).

From the foregoing theory the advantages of the explicit algorithm ($\theta = 0$ ub 3.1.5) can be seen. When applied to (3.1.8) and (3.1.11), the matrix H is eliminated from the theory, and (3.1.11) becomes

$$\hat{D}^n = D, \qquad (3.1.18)$$

so that the stiffness matrix K^n in (3.1.15) is simply the stiffness matrix K of the elastic analysis (2.1.8). As only the right-hand-side of the stiffness equation changes at each timestep, considerable savings in computer time can be made.

For the implicit algorithm, K^n will be symmetric only if an associated flow rule is used, i.e. Q = F and so a = b in (3.1.7). As already remarked, associated flow is not a realistic assumption for soils and rock.

The disadvantage of the explicit algorithm, of course, is its conditional stability; that is, there is a maximum size of the timestep Δt for which the method will converge. Cormeau (1975) derives limits for Δt for the explicit algorithm, associated flow, $\phi(F) = F$, and the standard yield surfaces to be described in the next section. In **FESTER,** the magnitude of the timestep is controlled by a parameter T which limits the maximum effective viscoplastic strain increment as a fraction of the total effective strain. This is subject to the new timestep not exceeding a fixed multiple of the preceding one. For full details, see Appendix and Owen & Hinton (1980), p.277. A further restriction on the maximum timestep size is introduced in section 4.4.

3.2 Yield surfaces

A general state of stress in three dimensions is defined by six components:

$$\sigma = (\sigma_X \sigma_Y \sigma_Z \tau_{XY}\ \tau_{XZ}\ \tau_{YZ})^T.$$

These may be resolved in an orientation in which there are no shear stresses, to give three principal stresses $\sigma_1, \sigma_2, \sigma_3$. The major and minor principal stresses are (taking compression positive)

$$\sigma_{maj} = \max\{\sigma_1 \sigma_2 \sigma_3\}$$
$$\sigma_{min} = \min\{\sigma_1, \sigma_2, \sigma_3\}. \qquad (3.2.1)$$

In plane strain, with z the out-of-plane direction, $T_{xy} = Ty_2 = 0$ and the three principal stresses are

$$\sigma_1 = \tfrac{1}{2}[\sigma_x + \sigma_y + \sqrt{(\sigma_x - \sigma_y)^2 + 4\tau^2_{XY}}]$$
$$\sigma_3 = \tfrac{1}{2}[\sigma_X + \sigma_Y - \sqrt{(\sigma_X - \sigma_Y)^2 + 4\tau^2_{xy}}] \qquad (3.2.2)$$
$$\sigma_2 = \sigma_Z.$$

Yield functions are drawn as surfaces in three-dimensional principal stress space, as in fig.1.3.1. However, the experimental determination of such a surface requires very complex apparatus. The usual method of measuring rock strength is in a triaxial test. A cylindrical rock sample is subjected to an all-round jacket pressure o_3, and an additional axial pressure $(\sigma_1 - \sigma_2)$ is increasingly applied until the rock yields. From such a test only the portion of the yield surface intersecting the plane $\sigma_2 = \sigma_3$ (called the triaxial plane) can be determined. A straight line approximation to this curve is provided by the Mohr-Coulomb yield criterion:

$$\sigma_{maj} = k\sigma_{min} + \sigma_c, \qquad (3.2.3)$$

see fig.3.2.1. Here, k is the triaxial stress factor, and σ_C is the unconfined compressive strength. They are related to the cohesion c and angle of internal friction φ by

$$k = \frac{1+\sin\varphi}{1-\sin\varphi}, \qquad \sigma_C = \frac{2c\cos\varphi}{1-\sin\varphi}. \qquad (3.2.4)$$

An alternative criterion was proposed by Hoek and Brown (1980) after analysing a large number of triaxial test results for a range of rock samples; it is

$$\sigma_{maj} = \sigma_{min} + \sqrt{m\sigma_C \sigma_{min} + s\sigma_C^2}, \qquad (3.2.5)$$

Here, is the unconfined comoressive strength of an intact rock sample, and s is a parameter $0 \le s \le 1$ to be estimated by the engineer, according to the degree of fracturing present in the rock mass. The unconfined compressive strength of the rock mass is then $\sqrt{s}\ \sigma_C$. . The parameter m plays a role

similar to that of the angle of friction in the Mohr-Coulomb model.

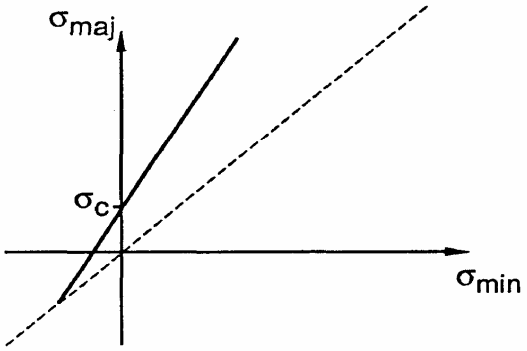

Figure 3.2.1

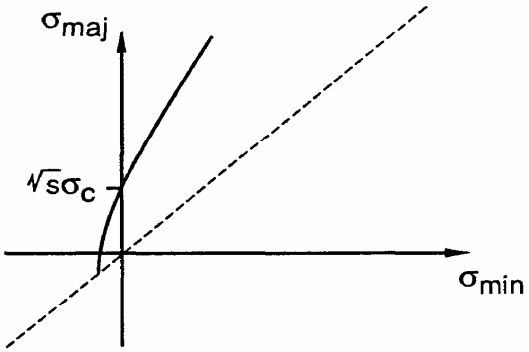

Figure 3.2.2

The location of the triaxial plane in three-dimensional principal stress space is shown in fig. 3.2.3, together with the hydrostatic axis $\sigma_1 = \sigma_2 = \sigma_3$, which is normal to the deviatoric planes (or π-planes)

$$\sigma_1 + \sigma_2 + \sigma_3 = \text{constant} \tag{3.2.6}$$

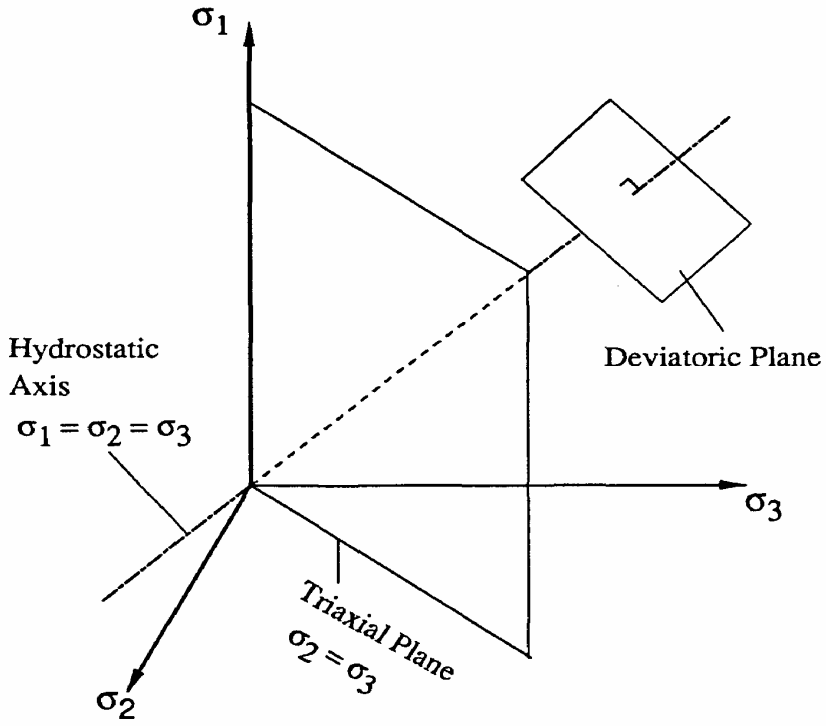

Figure 3.2.3

Yield surfaces in three dimensions are commonly written in terms of stress invariants; these will first be defined, insofar as they are relevant.

The first stress invariant is

$$I_1 = \sigma_1 + \sigma_2 + \sigma_3 = \sigma_x + \sigma_y + \sigma_Z \qquad (3.2.7)$$

The mean stress is $/_3 I_1$, and the deviatoric stresses are then

$$\sigma'_X = \sigma_X - {}^1/_3 I_1 \,,\ \sigma'_Y = \sigma_Y - {}^1/_3 I_1 \,,\ \sigma'_Z = \sigma_Z - {}^1/_3 I_1 \,.. \qquad (3.2.8)$$

The sceond deviatoric stress invariant is

$$J_2 = \frac{1}{2}\left(\sigma'^2_X + \sigma'^2_Y + \sigma'^2_Z\right) + \tau^2_{XY} + \tau^2_{XY} + \tau^2_{YZ}. \qquad (3.2.9)$$

An alternative expression for J_2 which can be derived is

$$J_2 = \frac{1}{6}\left[(\sigma_X - \sigma_Y)^2 + (\sigma_Y - \sigma_Z)^2 + (\sigma_Z - \sigma_X)^2\right] + \tau^2_{XY} + \tau^2_{XY} + \tau^2_{yZ}. \qquad (3.2.10)$$

The third stress invariant is

$$J_3 = \begin{vmatrix} \sigma'_X & \tau_{XY} & \tau_{XZ} \\ \tau_{XY} & \sigma_Y & \tau_{yZ} \\ \tau_{XZ} & \tau_{YZ} & \sigma'_Z \end{vmatrix}. \qquad (3.2.11)$$

A more meaningful quantity than J_2 is the Lode angle θ, defined by

$$\text{Cos } 3\theta = \frac{3\sqrt{3}}{2}\,\frac{J_3}{J_2\sqrt{J_2}}. \qquad (3.2.12)$$

The principal stresses σ_1, σ_2, σ_3 with σ_1, σ_2, σ_3 can now be written in terms of these invariants

$$\begin{pmatrix} \sigma_1 \\ \sigma_2 \\ \sigma_3 \end{pmatrix} = \frac{2\sqrt{J_2}}{\sqrt{3}} \begin{pmatrix} \sin(\theta + \frac{2\pi}{3}) \\ \sin\theta \\ \sin(\theta + \frac{4\pi}{3}) \end{pmatrix} + \frac{1}{3} I_1 \begin{pmatrix} 1 \\ 1 \\ 1 \end{pmatrix}. \qquad (3.2.13)$$

A full description of stress invariants can be found in Chen and Saleeb (1982).

The geometrical significance of I_1 J_2 and θ is shown in fig.3.2.4. Consider any point P with coordinates σ_1 σ_2 σ_3 Then the point A on the 1hydrostatic axis lying closest to P has coordinates $({}^1/_3 I_1,\ {}^1/_3 I_1\ {}^1/_3 I_1)$.

The distance PA is $\sqrt{2J_2}$,, and the angle $P\hat{A}Q$ (where Q is at (I_1 0 0)) is $\theta + \pi/6$ radians.

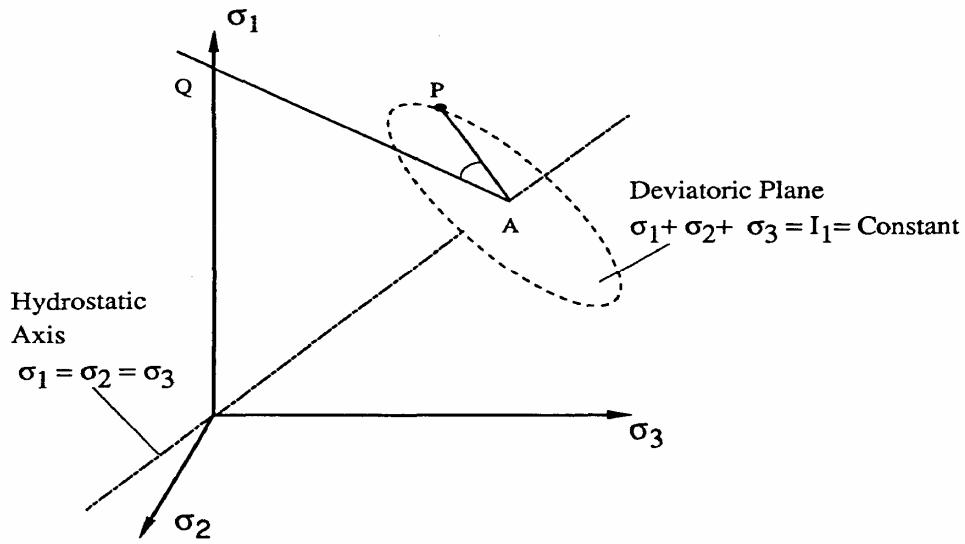

Figure 3.2.4

A final result which will be useful is

$$\sigma_1^2 + \sigma_2^2 + \sigma_3^2 = 2J_2 + \frac{1}{3}I_1^2 \qquad (3.2.14)$$

If the Mohr-Coulomb yield criterion (3.2.3) is applied to all possible stress combinations, the resulting surface is an irregular hexagonal cone around the hydrostatic axis - see Fig.3.2.5, which also shows a cross-section of the cone in the deviatoric plane. The sharp edges of the surface are at points where two of the principal stresses are equal.

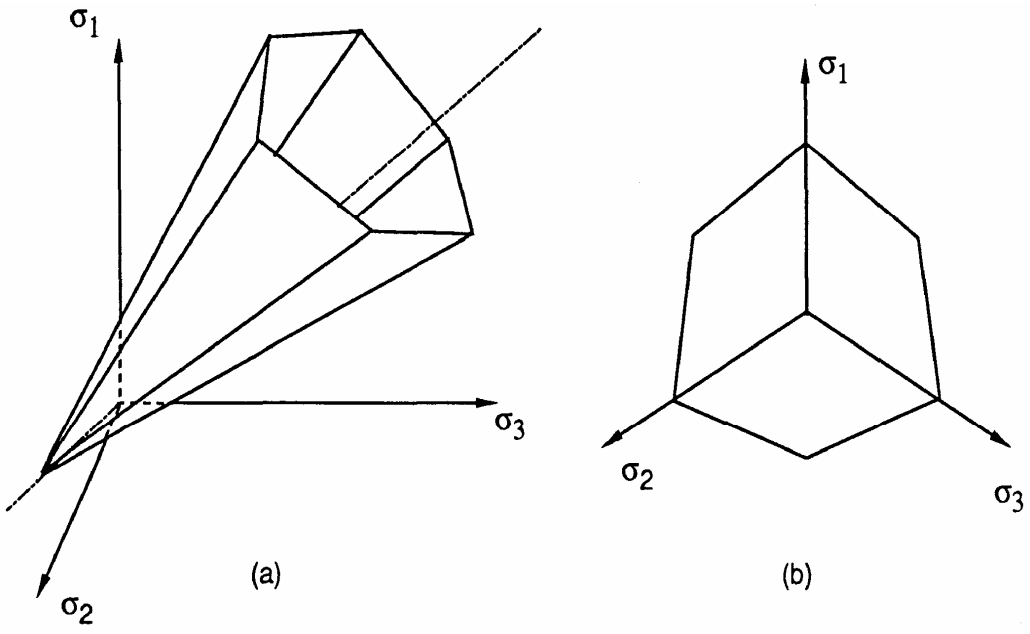

Figure 3.2.5

Substituting for the principal stresses in (3.2.3) from (3.2.13) gives the equation of the Mohr-Coulomb surface in terms of stress invariants

$$F(\sigma) = \frac{1}{3}(k-1)\, I_1 + \sqrt{J_2}[\sqrt{3}(k-1)\sin\theta + (k+1)\cos\theta - \sigma_C = 0. \qquad (3.2.15)$$

The Drucker-Prager yield criterion has a much simpler form for $F(\sigma)$, namely

$$F(\sigma) = \sqrt{J_2} - \alpha I_1 - p \qquad (3.2.16)$$

which defines a circular cone, as shown in fig.3.2.6. Its axial symmetry means that $F(\sigma)$ is independent of the Lode angle. The parameters α and p can be chosen so that the circular cross-section in the deviatoric p lane fits through either the outer or the inner apices of the Mohr-Coulomb hexagon.

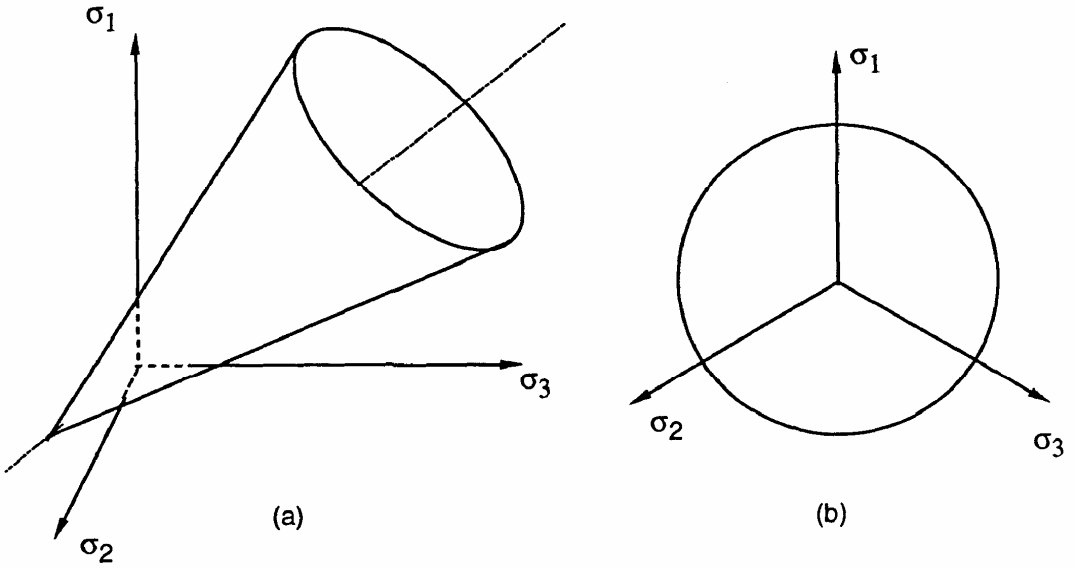

Figure 3.2.6

The other two classical yield surfaces are special cases of the above. The Tresca criterion is obtained from the Mohr-Coulomb by setting k = 1, and the Von Mises criterion is given by setting a = 0 in the Drucker-Prager; they are cylinders with cross-sections which are a regular hexagon and a circle respectively.

Careful experiments (e.g. Hoskins 1969) suggest that the true yield surface for rock materials has the general shape shown in 3.2.7.

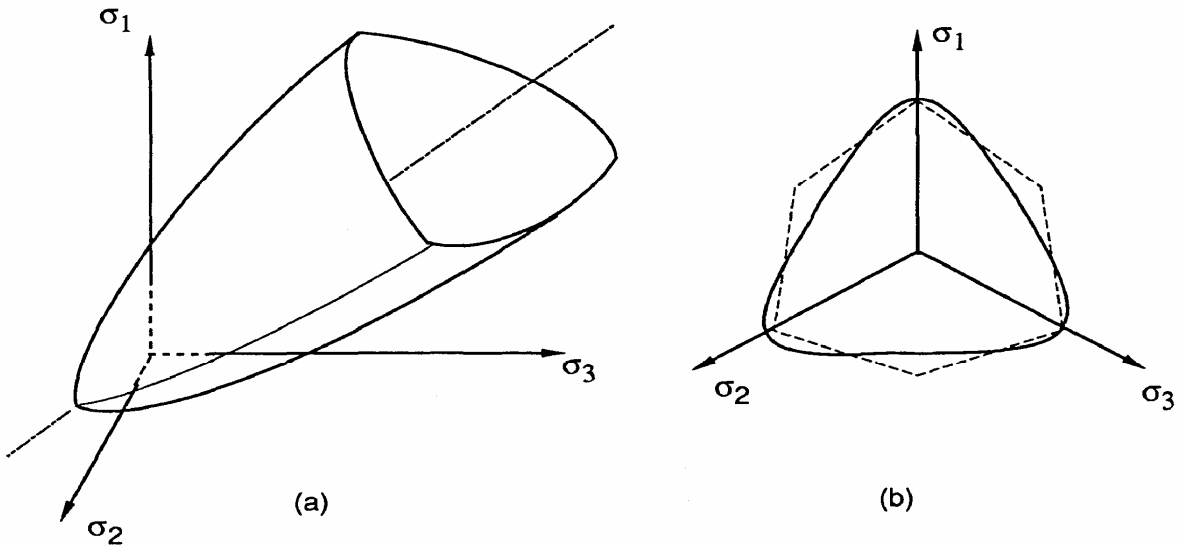

Figure 3.2.7

The Mohr-Coulomb hexagon is a reasonable approximation to the cross-sectional shape of this surface, but the sides of the surface should be curved, especially at low stresses, as in the Hoek-Brown criterion (fig.3.2.2). It is therefore proposed to extend the Hoek-Brown criterion (3.2.5) to three-dimensional stress space, giving a surface shown in fig.3.2.8.

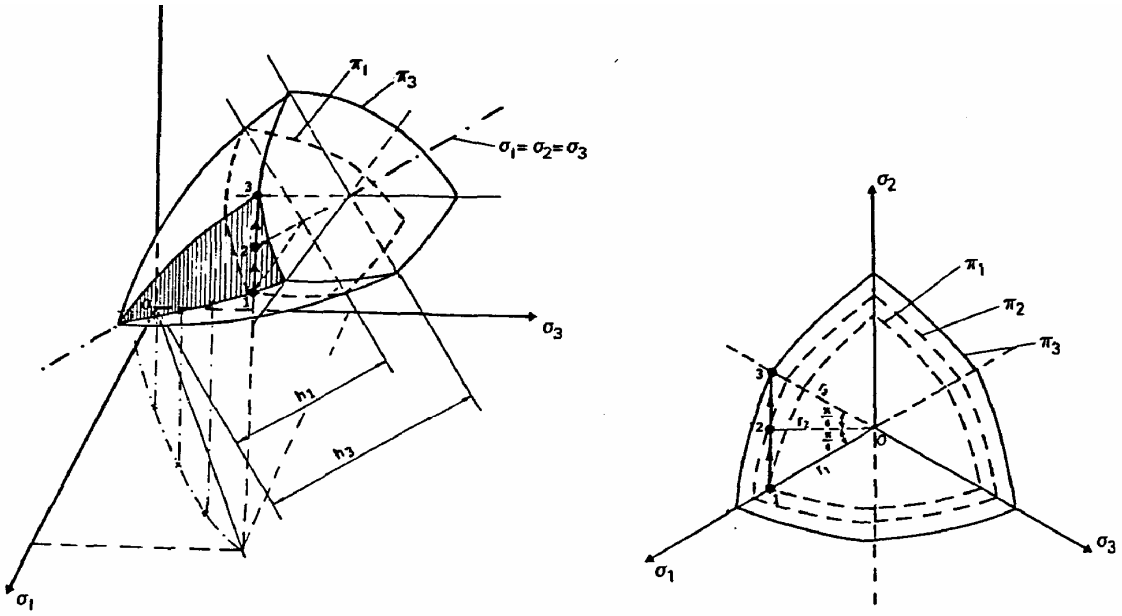

Fig.3.2.8

If a yield function F(o) is to be of use in the viscoplasticity algorithm with brittle plastic or strain-softening material, it is necessary that $F(\sigma) > 0$ when evaluated at any point outside the yield surface $F(\sigma) = 0$, and that the magnitude of F should be a measure of the distance from the point to the surface. This condition will be satisfied if F has the form

$$F(\sigma) = f(\sigma) - f_o \qquad (3.2.17)$$

where f_o is a constant indicating the strength of the material, and $f(\sigma)$ does not involve the strength. Then any point outside the yield surface would lie on a related surface with the same $f(\sigma)$ but a greater strength $f_o^* > f_o$.

The Mohr-Coulomb surface (3.2.15) is clearly of this form; it may be written more simply in terms of principal stresses from (3.2.3) as

$$F(\sigma) = \sigma_{maj} - k\sigma_{min} - \sqrt{s\sigma_c} \qquad (3.2.18)$$

where the parameter s, $0 \le s \le 1$, has been introduced to allow for the reduced strength of the fractured rock mass in situ, as compared with the strength of a rock sample measured in a triaxial test. (British Coal currently uses a similar parameter, namely writing $\frac{1}{f}\ \sigma_c$ instead of $\sqrt{s}\ \sigma_c$. The choice of s is made here for consistency with the Hoek-Brown model. See also section 3.4, where the concept of brittleness is introduced.)

The Hoek-Brown criterion (3.2.5) is not so readily transformed, but by solving for $s\sigma_c^2$ the yield surface may be written (Reed 1986a)

$$F(\sigma) = \sqrt{(\sigma_{maj} - \sigma_{min})^2 - m\sigma_c\,\sigma_{min}} - \sqrt{s}\ \sigma_c \ . \qquad (3.2.19)$$

Note that $\sqrt{s}\ \sigma_c$ is the unconfined compressive strength (fig .3.2.2).

Other yield functions have been proposed by Kim and Lade (1984), and Matsuoka and Nakai (1974) to produce curved surfaces as in fig.3.2.7, but these do not satisfy the above condition on $F(\sigma)$; Burd (1986) has diagrams of the 'extraneous' surfaces $F(\sigma) = 0$ lying above the main yield surface.

A general criterion used by Zienkiewicz and Pande (1975) is

$$F(\sigma) = q^2 - \alpha_2 P^2 + \alpha_1 P - \alpha_0 \qquad (3.2.20)$$

where

$$q = \frac{1}{2\gamma}\left[(\gamma+1) - (\gamma-1)\frac{3\sqrt{3}\ J_3}{2J_2\sqrt{J_2}}\right]\sqrt{J_2} \text{ and } p = I_1 \ .$$

This has not been used in FESTER for practical reasons; the four material parameters α_0 , α_1, α_2 , γ would require extensive and sophisticated testing for their measurement, and this is not a practical possibility especially given the difficulty of taking representative core samples from an underground rock mass with large in situ stresses.

In FESTER the emphasis has been on models with a minimum of material parameters, which should have physical significance and be easily measured or estimated. For this reason the two rock models which have been employed are:

(i) the Mohr-Coulomb yield surface (equation (3.2.18), figure 3.2.5);
(ii) The Hoek-Brown yield surface (equaiton (3.2.19), figure 3.2.8).

So far, the discussion has assumed ideal plasticity, that is, the yield surface remains fixed throughout the deformation. The question of brittleness and strain-softening, in which there is a sudden or gradual loss of strength, is dealt with in section 3.4. First, however, we discuss the choice of flow rule.

A good recent review of the experimental and theoretical aspects of soil modelling is given by Dyer et al (1986).

3.3 Flow rules

The flow rule (3.1.4) is defined by the choice of plastic potential function $Q(\sigma)$. Prévost and Höeg (1975) have shown that for strain-softening materials, $Q(\sigma)$ must be a convex surface, as is required for $F(\sigma)$ in ideal plasticity. Hence, we may choose a plastic potential from the range of functions described in the previous section.

The flow rule is associated if $Q \equiv F$. It may be termed 'fully non-associated' if the flow vector $b = \dfrac{\partial Q}{\partial \sigma}$ lies in the deviatoric plane I_1 = constant. In this latter case, it follows from the definition of volumetric strain.

$$\varepsilon_V = \varepsilon_X + \varepsilon_Y + \varepsilon_Z \qquad (3.3.1)$$

and the flow rule (3.1.4) that the volumetric plastic strain increment is zero, i.e. there is no plastic dilation of the rock. Such a fully non-associated flow rule predicts displacements which are of the order observed in practice.

A flow rule which has been widely used in conjunction with the Mohr-Coulomb yield criterion, is obtained by replacing the angle of internal friction φ with an angle of dilation ψ, $0 \leq \psi \leq \varphi$ in defining $Q(\sigma)$. Thus, at the one extreme $\psi = \varphi$ we have an associated flow rule, while at the other $\psi = 0$ gives a Tresca surface for $Q(\sigma)$ and the rule is fully a

non-associated. In fig.3.3.1 the cross-section of the yield surface in the deviatoric plane is shown, together with a field of flow lines indicating the direction of b at points outside the surface. A generic $Q(\sigma)$ is drawn in dashed lines; for the case $\psi = 0$ its cross-section is a regular hexagon.

This approach is not followed in FESTER, for a number of reasons. Firstly, there is the question of the singularities at the corners of the hexagon, and the resultant sudden change in direction of b along lines emanating from these corners. Formulae have been proposed for 'smoothing off' these corners (e.g. Sloan and Booker 1986), but these of necessity introduce new parameters. The problem is compounded because the flow rule tends to direct the stress state precisely towards these corners, especially in problems having axial symmetry. Reed (1986b) has shown how in the axisymmetric problem of a circular tunnel in an infinite rock mass,

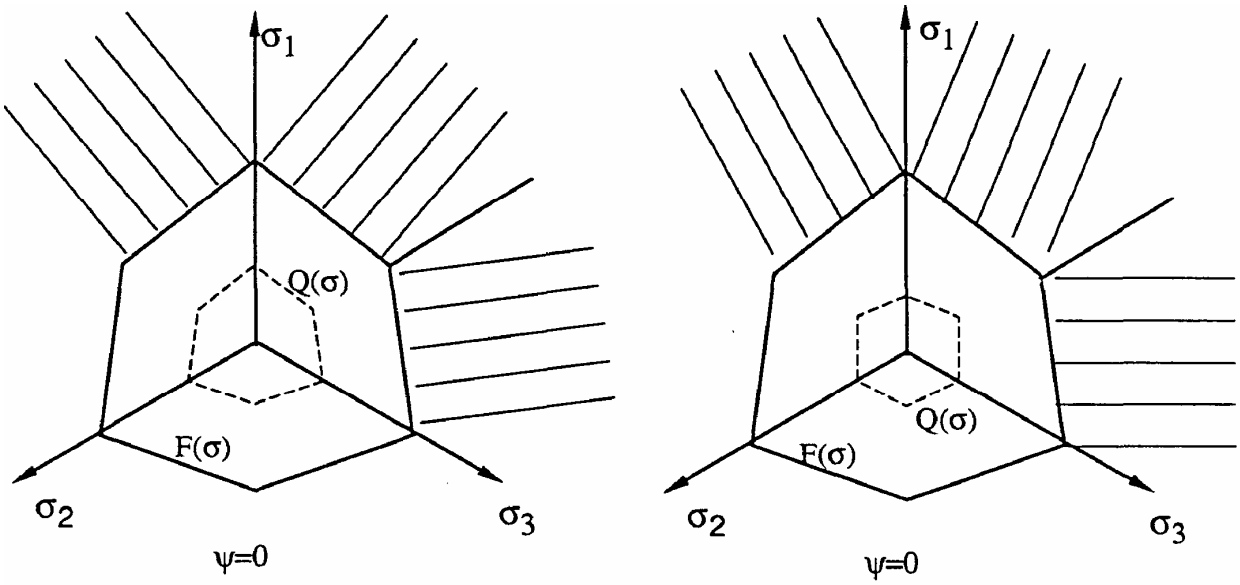

Figure 3.3.1

an inner plastic zone arises in which $\sigma_z = \sigma_\theta$. Koiter (1953) shows how these singularities may be handled in plasticity theory, namely as the intersection of two yield surfaces, with contributions to the flow rule from each surface, but it is arguable whether 'smoothing off the corners' approaches this in the limit.

A final, pragmatic reason for not using the Mohr-Coulomb-type flow rule, is the complexity of forming the Hessian matrix of second partial derivatives of $Q(\sigma)$, required in (3.1.7), especially when the function is described in terms of stress invariants, i.e. (3.2.15).

In FESTER the plastic potential is chosen independently of the yield function; the function chosen is that of Drucker-Prager, equation 3.2.16. Since only derivatives of $Q(\sigma)$ are used in the viscoplasticity algorithm, the constant term may be omitted and the function written

$$Q(\sigma) = \sqrt{J_2} - \alpha I_1 \qquad (3.3.2)$$

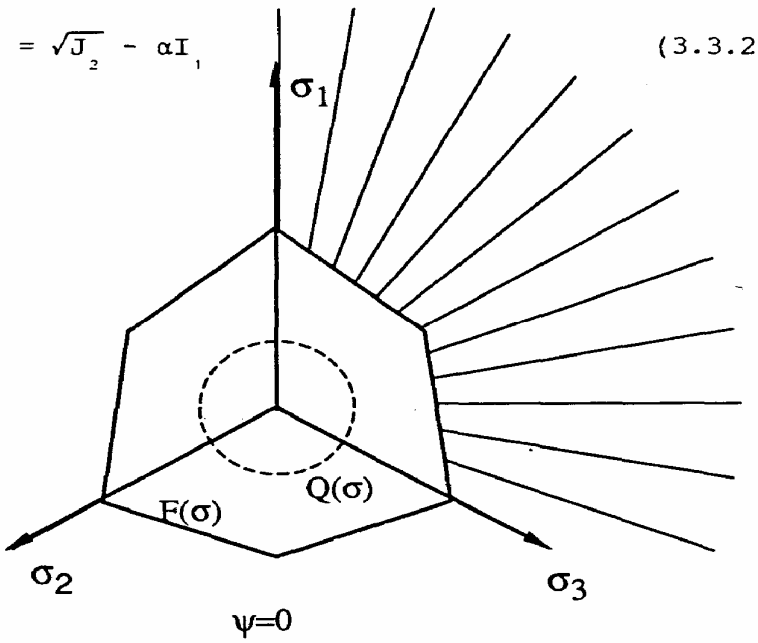

Figure 3.3.2

The generic surface is a circular cone, shown in fig.3.2.6, and the resulting flow field in the deviatoric plane is shown in fig.3.3.2; there is now no problem of singularities. The flow vectors act towards the hydrostatic axis. This is similar to the flow rule used in critical state theory, where the flow in the strain-softening part of the curve is towards the hydrostatic p-axis (Schofield and Wroth 1968, p.150).

This flow rule is used with the Mohr-Coulomb as well as Drucker-Prager yield surface. A fully non-associated flow rule is obtained by setting the dilation parameter $\alpha = 0$ in (3.3.2). There is no value of a which will give associated flow for the Mohr-Coulomb model, but an upper limit on α is

$$\alpha_{max} = \frac{2\sin\varphi}{\sqrt{3}(3-\sin\varphi)} = \frac{k-1}{\sqrt{3}(k+2)} \qquad (3.3.3)$$

in which case $Q(\sigma)$ generates a family of cones with the same apex angle as the yield surface; in the deviatoric plane the Drucker-Prager circle coincides with the outer apices of the Mohr-Coulomb hexagon. The performance of this flow rule is discussed in Reed (1988b).

For the Hoek-Brown model, a similar simplified flow rule may be constructed, in which the plastic potential $Q(\sigma)$ is independent of the Lode angle θ (i.e. it is a volume of revolution around the hydrostatic axis), but has a curved profile in the triaxial plane matching that of the Hoek-Brown surface. It is obtained by writing (3.2.19) in terms of stress invariants, evaluating $F(\sigma)$ at the angle $\theta=0$ (giving a 'mean surface' between the inner and outer apices), omitting the strength constant, scaling and introducing a variable dilation parameter α. This produces

$$Q(\sigma) = \sqrt{J_2 + \alpha\sigma_c \left(\sqrt{J_2} - \frac{1}{3} I_1\right)} \qquad (3.3.4)$$

where $\alpha = \frac{1}{4}m$ for 'quasi-associated flow', and $\alpha = 0$ for zero plastic dilation (in which case the rule is equivalent to 3.3.2).

The derivatives of $Q(\sigma)$ are easily found, and are set out in section 4.1. A similar surface has also been used by Pan and Hudson (1988).

3.4 Brittleness and strain-softening

Thus far in this section it has been assumed that the yield surface $F(\sigma)$ remains constant throughout the deformation. In practice, rock does not have this ideal plastic nature, but instead shows a rapid drop in strength upon yield. FESTER models this behaviour by using different material parameters in testing for initial yield and for the subsequent viscoplasticity algorithm.

Thus, for the Hoek-Brown model, initial yield is tested using (3.2.5) with the virgin parameters m, s, but the yield surface (3.2.20) is defined by residual parameters m', s'. This is consistent with the way Hoek (1983) proposed modelling brittle plastic rock with this criterion. The unconfined compressive strength σ_c is that measured for a small rock sample containing no joints. The parameters s and s' are in the range $0 \le s' \le s < 1$ and indicate the degree of jointing in the rock mass before and after failure. The corresponding unconfined compressive strengths of the rock mass are then $\sqrt{s'}\,\sigma_C$ and, $\sqrt{s}\,\sigma_C$ found by setting $\sigma_{min} = 0$ in (3.2.5).

In FESTER this dea has been carried over to the Mohr-Coulomb model, using (3.2.18):

$$F(\sigma) = \sigma_{maj} + k\sigma_{min} - \sqrt{s}\,\sigma_c$$

for initial yield, with residual parameters k' and s'.

This elastic-brittle plastic model assumes that the failure mechanism is a catastrophic micro-cracking in the rock, causing the sudden loss of strength. If a gradual drop in strength is required, governed by the

extent of the plastic deformation, then an elastic-strain softening model must be used. Strain-softening models were originally developed by using a negative value for the strain-hardening parameter in the elasto-plastic algorithm used for strain-hardening materials such as metals, but this has considerable problems with numerical stability (Thomas 1984). This is a major reason why the elasto-viscoplastic algorithm was used in FESTER.

For a strain-softening model, the general form of the yield function in (3.2.17) is altered by introducing a dependence upon a strain-softening parameter K:

$$F(\sigma, k) = f(\sigma) - f_0(K) \qquad (3.4.1)$$

The value of K depends on the extent of plastic strain; this is conveniently measured by the generalized plastic strain, $\bar{\varepsilon}_p$. For example a parabolic drop in strength from $\sqrt{s}\,\sigma_c$ to $\sqrt{s'}\,\sigma_c$, as shown in fig. 3.4.1,

Figure 3.4.1

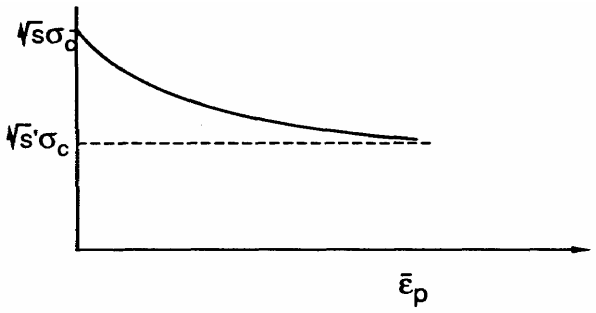

would be given by

$$f_0(K) = \left[\frac{A\sqrt{s} + \bar{\varepsilon}_p \sqrt{s'}}{A + \bar{\varepsilon}_p} \right] \sigma_c \qquad (3.4.2)$$

where A is parameter controlling the rapidity of the loss of strength. This model is used by Thomas (1984).

It will be seen that the brittle plastic model used in FESTER is an extreme case of (3.4.2), with A = 0.

3.5 Plane of weakness

The final aspect of rock behaviour which is modelled in **FESTER** is anisotropy, more specifically the presence of a plane or orientation of weakness. This anisotropy is introduced in two ways: orthotropic elastic properties, and extra plastic yield conditions.

The plane of weakness arises from the laminated nature of the rock mass, created during sedimentation. In plane strain situations it extends in the out-of -plane direction, and at an angle P to the x-axis in the

xy-plane. Fig. 3.5.1 illustrates such a rock stratum.

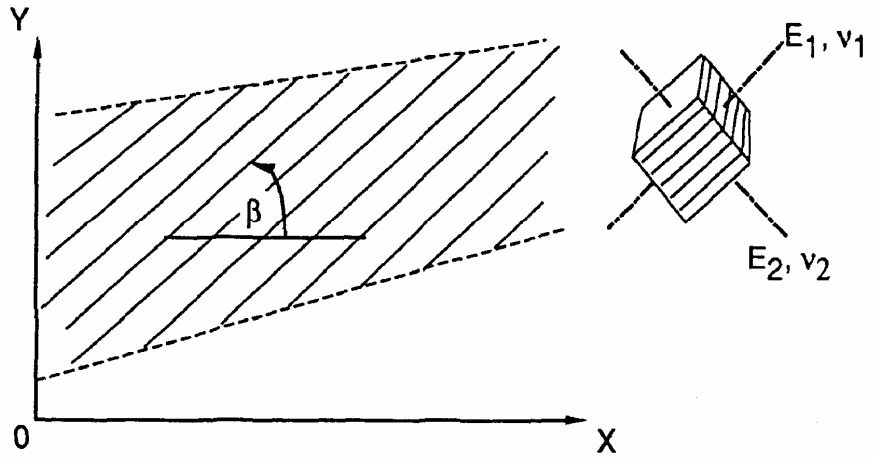

Figure 3.5.1

A sample cut from this rock will exhibit different elastic behaviour depending upon the direction of loading. This orthotropic elasticity is defined by five parameters: E_1, ν_1, are the Young's modulus and Poisson's ratio in the direction parallel to the plane of weakness; E_2, ν_2 are the corresponding properties in the direction normal to the plane, and G is the shear modulus. The orthotropic elastic constitutive matrix D for plane strain, replacing that for isotropy in (2.1.2), is (Zienkiewicz 1977):

$$D = T D' T^T \tag{3.5.1}$$

where

$$D' = \frac{E_2}{(1+\nu_1)(1-\nu_1-2n\nu_2^2)} \begin{pmatrix} n(1-n\nu_2^2) & n\nu_2(1+\nu_1) & 0 & n(\nu_1+n\nu_2^2) \\ n\nu_2(1+\nu_1) & 1-\nu_1^2 & 0 & n\nu_2(1+n\nu_1) \\ 0 & 0 & m(1+\nu_1)(1-\nu_1-2n\nu_2^2) & 0 \\ n(\nu_1-n\nu_2^2) & n\nu_2(1+\nu_1) & 0 & n(1-n\nu_2^2) \end{pmatrix}$$

(3.5.2)

with $n = \frac{E_1}{E_2}$ and $m = \frac{G}{E_2}$.

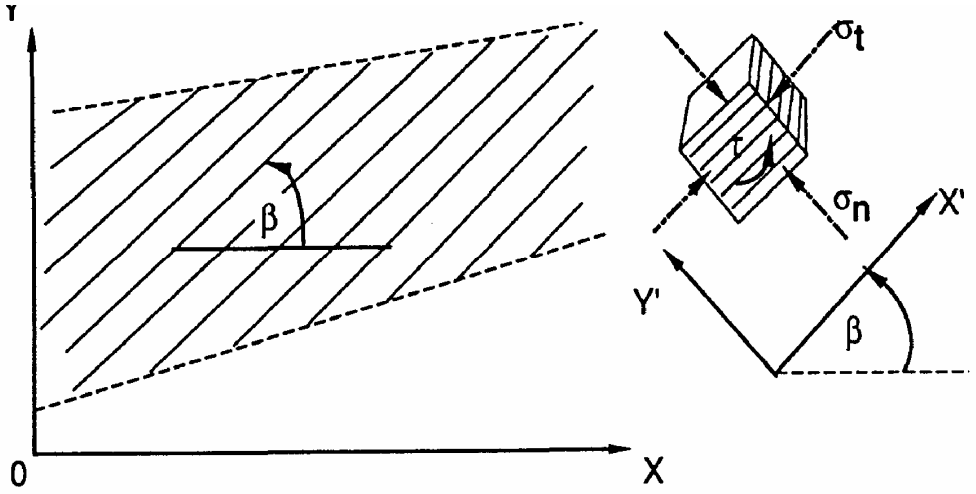

Figure 3.5.2

D' is the D-matrix in the x'y' coordinate system oriented with the plane of weakness (fig.3.5.2); it is transformed to the cartesian D-matrix by (3.5.1), where the transformation matrix T is

$$T=\begin{bmatrix} \cos^2\beta & \sin^2\beta & -2\sin\beta\sin\beta & 0 \\ \sin^2\beta & \cos^2\beta & 2\sin\beta\sin\beta & 0 \\ \sin\beta\sin\beta c & -\sin\beta\sin\beta c & \cos^2\beta-\sin^2\beta & 0 \\ 0 & 0 & 0 & 1 \end{bmatrix} \qquad (3.5.3)$$

Recall from section 2.1 that in this notation the out-of-plane stress and strain are located in the fourth row of the stress/strain vectors. Resolving these cartesian stresses in the x'y' coordinate system gives σ_n (the stress normal to the plane of weakness), σ_t (the stress tangential to the plane) and shear stress τ as

$$\begin{aligned} \sigma_n &= \sin^2\beta\sigma_x + \cos^2\beta\sigma_y - 2\sin\beta\cos\beta\tau_{xy} \\ \sigma_t &= \sin^2\beta\sigma_x + \sin^2\beta\sigma_y - 2\sin\beta\cos\beta\tau_{xy} \qquad (3.5.4) \\ \tau &= \sin\beta\cos(\sigma_y-\sigma_x) + (\cos^2\beta\sin\beta)\tau_{xy}. \end{aligned}$$

We now consider the circumstances in which sliding will occur along the planes of weakness. By the theory of limiting friction, sliding occurs if

$$|\tau| \geq \sigma_n \tan\varphi_j + c_j \qquad (3.5.5)$$

where φ_j is an angle of friction and c_j a cohesion associated with the jointing. A further criterion is that the rock cannot support a tensile

Stress across the joints, i.e. the rock will break if $\sigma_n < 0$.

In FESTER these two criteria provide additional yield functions, which with their own flow rules can also contribute to the plastic strain rate. The no-slip criterion has yield function $F_1,(\sigma)$ and plastic potential $Q_1,(\sigma)$ defined by

$$\begin{aligned} F_1(\sigma) &= |\tau| - \sigma_n \tan\varphi_j - c_j \\ Q_1(\sigma) &= |\tau| - \sigma_n \tan\psi_j \end{aligned} \tag{3.5.6}$$

where ψ_j is an angle of dilation. The no-tension criterion has yield function $F_2(\sigma)$ and plastic potential $Q_2(\sigma)$:

$$F_2(\sigma) = Q_2(\sigma) = -\sigma_n . \tag{3.5.7}$$

The conventional flow rule is used, as in (3.1.4):

$$\dot{\varepsilon}^i_{vp} = \gamma_j \; < \Phi(F_i) > \frac{\partial Q_i}{\partial \sigma} \quad i = 1,2 \tag{3.5.8}$$

where γ_j is a fluidity parameter for the jointing.

We will say that the rock has cracked if either of these flow rules become active. This cracking process is independent of the plastic yield of the rock mass described in previous sections - that is, at a given Gauss-point the rock may have cracked but not yielded plastically, or vice versa, or neither, or both. The way in which this cracking model (which is based on the multilaminate rock model proposed by Zienkiewicz and Pande 1977) is incorporated into the viscoplasticity algorithm, is described in the next section.

3.6 Models used in FESTER

We conclude this chapter by filling in the details of the viscoplasticity algorithm in FESTER. The existence of more than one yield surface is easily handled; each active flow rule of the general form

$$\dot{\varepsilon}^i_{vp} = \gamma^i < \Phi^i(F_i) > \frac{\partial Q_1}{\partial \sigma} \tag{3.6.1}$$

contributes a viscoplastic strain increment. The total viscoplastic strain rate is then

$$\dot{\varepsilon}^i_{vp} = \sum_i \dot{\varepsilon}^i_{vp} \tag{3.6.2}$$

and (3.6.1) and (3.6.2) replace (3.1.4) in the viscoplasticity theory. The other change is that the matrix H in (3.1.7) now becomes a sum of matrices

H_i from each active flow rule. It is usual to choose the functions $\Phi(F)$ in the flow rule as

$$\Phi(F) = \frac{f(\sigma) - f_o}{f_o} \qquad (3.6.3)$$

when $F(\sigma)$ has the general form (3.4.2). However, for rock strata with very low residual strength, f_o will be close to zero, and (3.6.3) will cause very large plastic strain increments, giving rise to numerical instability. Therefore, it is the practice in FESTER to use

$$\Phi(F) = F \, . \qquad (3.6.4)$$

The drawback to this is that Φ is not dimensionless, and thus the viscosity parameter γ must be scaled according to the units of stress being used.

A final yield criterion has been added in FESTER, partly to model realistic rock behaviour and partly to cure a numerical instability which may arise. Even isotropic rock with no planes of weakness can support only a very limited tensile stress; it may be unrealistic for stress states to lie on parts of the yield surfaces in figs.3.2.5 or 3.2.8 where the minor principal stress is negative. In FESTER a small negative tensile strength σ_{ten} may be specified, and if $\sigma_{min} < \sigma_{ten}$ then the small-tension flow rule defined by

$$F(\sigma) = Q(\sigma) = \sigma_{ten} - \sigma_{min} \qquad (3.6.5)$$

with $\Phi(F) = F$ and the same fluidity parameter as for plastic yield, becomes active.

This flow rule may come into play even in problems where the stresses do not theoretically become negative, if there is a large drop of strength on yield, a low residual strength and an unsupported excavation. In this case, when at a certain time a new rock element away from the excavation yields, there is a large stress redistribution which can push elements close to the rock face, where all the stresses are low, into negative parts of the stress space temporarily. The numerical method will diverge if a stress state finds itself in a deviatoric plane behind the apex of the yield surface; a Drucker-Prager flow rule with low dilation will not move such a point back to the surface. This small-tension criterion is used by, for example, Cramer and Wunderlich (1981).

To summarize, then, there are a total of nine types of material model used in FESTER:

1. Linear elastic structure (no in situ stresses), isotropic.
2. Linear elastic rock, isotropic.
3. Linear elastic orthotropic rock.
4. Viscoplastic isotropic rock with Mohr-Coulomb yield.

5. Viscoplastic isotropic rock with Hoek-Brown yield.

6. Viscoplastic orthotropic rock with Mohr-Coulomb yield.

7. Viscoplastic orthotropic rock with Hoek-Brown yield.

8. Viscoplastic isotropic rock with Drucker-Prager yield.

9. Elastic joint element.

The Drucker-Prager material type is available for theoretical studies- with this material it is possible to have associated flow, with the flow rule (3.3.2).

Details of the material parameters required for each model are given in the Appendix.

CHAPTER 4 IMPLICIT ALGORITHM; PRACTICAL ASPECTS

4.1 Calculation of H

In the implicit algorithm, as described in section 3.1, it is necessary to form the viscoplasticity matrix $\hat{D}^n$, at each element integration point and at each timestep. $\hat{D}^n$ is defined in (3.1.11), which can be generalized to

$$\hat{D} = (D^{-1} + \theta\Delta t \sum_i \dot{H}^i)^{-1} \qquad (4.1.1)$$

where more than one flow rule is active. (The superscript indicating the n'th timestep is now omitted, for convenience). For each flow rule the matrix

$$H = \gamma\left\{\Phi(F)\frac{\partial b^T}{\partial\sigma} + \frac{d\Phi}{dF} b\, a^T\right\} \qquad (4.1.2)$$

must be formed (equation 3.1.7). For completeness, some of these expressions will now be given, in forms suitable for computation.

The Drucker-Prager plastic potential (3.3.2) is used with the flow rule for the rock mass. Performing the differentiations gives the following results for

$$Q(\sigma) = \sqrt{J_2} - \alpha I_1 :$$

Let $c = \dfrac{\partial\sqrt{J_2}}{\partial\sigma} = \dfrac{1}{2\sqrt{J_2}}(\sigma'_x \;\; \sigma'_y \;\; 2\tau_{xy} \;\; \sigma'_z)^T$ and $m = \dfrac{\partial I_1}{\partial\sigma} = (1 \;\; 1 \;\; 0 \;\; 1)^T$

Then

$$b = \frac{\partial Q}{\partial\sigma} = c - \alpha m, \qquad (4.1.3)$$

and

$$\frac{\partial b^T}{\partial\sigma} = \frac{1}{\sqrt{J_2}}\left[A - c c^T\right] \quad \text{where} \quad A = \frac{1}{6}\begin{bmatrix} 2 & -1 & 0 & -1 \\ -1 & 2 & 0 & -1 \\ 0 & 0 & 6 & 0 \\ -1 & -1 & 0 & 2 \end{bmatrix}.$$

For Hoek-Brown materials, using the plastic potential (3.3.4), the corresponding derivatives are

$$b = \frac{\partial Q}{\partial\sigma} = \frac{1}{2Q(\sigma)}\left[2\sqrt{J_2}\, c + \alpha\sigma_C\left(c - \frac{1}{3}m\right)\right]$$

and (4.1.4)

$$\frac{\partial b^T}{\partial\sigma} = \frac{1}{Q(\sigma)}\left[A + \frac{\alpha\sigma_c}{2\sqrt{J_2}}(A - c\,c^T) - b\,b^T\right]$$

with A, c, m defined as before.

The Mohr-Coulomb and Hoek-Brown yield functions are defined in (3.2.19) and (3.2.20) in terms of the major and minor principal stresses. The vector a is found from the chain rule:

$$a = \frac{\partial F}{\partial \sigma} = \frac{\partial F}{\partial \sigma_{min}} \frac{\partial \sigma_{min}}{\partial \sigma} + \frac{\partial F}{\partial \sigma_{maj}} \frac{\partial \sigma_{maj}}{\partial \sigma} . \qquad (4.1.5)$$

The principal stresses are defined in (3.2.1) - (3.2.2), and their derivatives are

$$\frac{\partial \sigma_1}{\partial \sigma} = (p\ ,\ 1-p,\ r\ ,\ 0)^T$$

$$\frac{\partial \sigma_3}{\partial \sigma} = (1-p,\ p\ ,-r\ ,\ 0)^T \qquad (4.1.6)$$

$$\frac{\partial \sigma_z}{\partial \sigma} = (\ 0\ ,\ 0\ ,\ 0\ ,\ 1)^T$$

where $p = \frac{1}{2}\left[1 + \frac{\sigma_x - \sigma_y}{\sigma_1 - \sigma_3}\right]$ and $r = \frac{2\tau_{xy}}{\sigma_1 - \sigma_3}$.

There will be a sudden change of direction in a when two principal stresses are equal, but as the flow rule does not direct stress states towards these corners of the yield surface it has not been found necessary to introduce any smoothing here.

For the small-tension yield criterion (3.6.4), the first and second derivatives of σ_{min} are required. The first derivatives are given above, and the Hessian matrix of second derivatives is

$$\frac{\partial a^T}{\partial \sigma} = \frac{2}{(\sigma_x + \sigma_y - 2\sigma_3)^3} d\, d^T \qquad (4.1.7)$$

where $d = (-\tau_{xy}, \tau_{xy}, \sigma_x - \sigma_y, o)^T$ if $\sigma_{min} = \sigma_3$,

and $\frac{\partial a^T}{\partial \sigma} = 0$ if $\sigma_{min} = \sigma_z$ (which is unlikely) .

The cracking flow rules are given in (3.5.6)-(3.5.7). Notice from these and (3.5.4) that each $F(\sigma)$ and $Q(\sigma)$ is a linear combination of the stress components, so that the first derivatives a and b will be constant vectors, and the Hessian matrix $\frac{\partial b^T}{\partial \sigma} \equiv 0$.

4.2 Large displacements

The strain-displacement relationships (2.1.3) are in fact approximations ignoring second- and higher-order terms in e, and for this reason the theory describved in the preceding chapters is based on the assumption of small strains.

A further assumption that has been implicit in the theory is of small displacements; this is assumed when the Cartesian derivatives of the shape functions (terms such as $\partial N_i/\partial x$) are evaluated for the matrix B in (2.1.6). This process uses the nodal coordinates $x(^e)$ which has been assumed fixed, even though the nodes are being displaced. The assumption can be avoided by adding the current nodal displacements $d(^e)$ to $x»^e)$ before using this vector in forming the matrix B. Then B will no longer be constant, but will change slightly at each timestep. This is not a problem in the implicit algorithm, since here $\hat{D}$ is also changing, and the stiffness matrix is reformulated at each timestep.

This refinement has been tested in FESTER, and has a small effect on the results; for example, in an axisymmetric tunnel problem using the Hoek-Brown criterion, a wall displacement of 16.366mm with constant B became 16.356mm when the effect of the displacements was taken into account, and the stresses close to the tunnel wall dropped slightly. (The tunnel radius was 4m.)

However, this minor modification can produce unexpected results if a new user is experimenting with the program on a simple linear elastic problem, for which he knows the analytic solution. As the effect of the. refinement is small, it has been decided to avoid potential confusion and omit the refinement.

Ideally, of course, large strain theory should be included in FESTER, and this major modification will be made in a future version of the program.

4.3 Solution techniques

This section briefly mentions the method of solving the global incremental stiffness equation (3.1.15). The matrix K^n is large, sparse and banded. It will be symmetric if either

(i) an elastic analysis is being performed;

(ii) the explicit viscoplasticity algorithm (with constant B) is used;

or (iii) only associated flow rules are used, so that b = a in (3.1.7).

In FESTER, the initial elastic solution is performed using the original FINEPACK routine FRONT. This is written for a symmetric matrix K (so that only half the matrix need be stored) and uses the frontal solution method.

which is a variant of Gaussian elimination in which the assembly of K from the element stiffness matrices $k^{(e)}$ is interleaved with the elimination process; the advantage of this is that the whole assembled matrix does not need to be held in store. This routine also keeps a record of the elimination process on scratch files, so that much of the work can be avoided in any re-solutions using the same stiffness matrix with a different right-hand-side. Matrix elements are held in a one-dimensional array GSTIF, so that element kij is linked to GSTIF(NFUNC), where

$$\mathrm{NFUNC}(I,J) = (J^{*}J - J)/2 /+ I. \qquad (J \geq I) \qquad (4.4.1)$$

The ordering of this storage is illustrated in fig.4.4.l(a).

If the explicit algorithm (0=0) is employed, this subroutine is used in the subsequent timestepping, and the extra efficiency in re-solutions is taken advantage of.

For the implicit algorithm, subroutine FRONT has been generalized to produce a routine AFRONT which uses the frontal method on an unsymmetric

$$\begin{pmatrix} 1 & 2 & 4 & 7 & 11 \\ & 3 & 5 & 8 & \downarrow \\ & & 6 & 9 & \\ & & & 10 & \end{pmatrix} \qquad \begin{pmatrix} 1 & 4 & 9 & \\ 2 & 3 & 8 & \uparrow \\ 5 & 6 & 7 & 14 \\ 10 & 11 & 12 & 13 \end{pmatrix}$$

(a) (b)

Fig. 4.4.1

matrix K. The ordering in GSTIF used to hold the upper and lower triangular parts of K is shown in fig.4.4.l(b); this is achieved by the function

$$\mathrm{NFUNC}(i,j) = (\mathrm{MAX}\{i,j\} - 1)^2 + \mathrm{MAX}\{j - i, 0\}. \qquad (4.4.3)$$

There is no partial or full pivoting, so it is possible that numerical errors could arise in the solution if K is ill-conditioned. A check on this is provided by printing out the largest and smallest pivots encountered during the solution process; a large difference in the magnitudes of these would suggest that the results from the program were suspect.

There has recently been much work done on using iterative solution methods such as conjugate gradients in finite element computations. It is planned to investigate the use of an iterative method applicable to unsymmetric matrices to make the implicit algorithm in FESTER more efficient for large problems.

4.4 Undershoot

In the conventional viscopiasticity algorithm, the final solution obtained will be dependent on the timestepping regimen that is used; however, the solutions will approach that for an elasto-plastic model (in which stress states doe not exceed the yield surface) as the individual timesteps are progressively reduced in size (or, equivalently, as the viscosity parameter y is reduced). This is because any individual visco-plastic strain increment $\Delta\varepsilon^{n}_{vp}$ can be made arbitrarily small as $\gamma\Delta t_n \rightarrow 0$.

(see equations 3.11.4, 3.1.8). This is not the case with the brittle rock model, where there is a minimum finite distance which a stress state must lie outside the residual yield surface when it first yields plasticically. In practice this can cause the phenomenon of 'undershoot', in which yielded stress states move inside the yield surface to the elastic region during the timestepping, instead of coming to rest on the surface, and this cannot be cured by taking smaller timesteps. The technique used in FESTER to counter this problem is to allow 'reverse plastic straining' - that is, the flow rule 3.1.4 is used with $\phi(F) = F$ even when σ^n lies in the elastic region $F(\sigma) < 0$, if yield has already occurred. This gives a 'negative' plastic strain rate ε^{-n}_{VP} which in (3.1.10) will produce a stress increment to move σ^{n+1} a back up to the yield surface. A similar problem occurs in elasto-plastic algorithms where Gauss points unload and become elastic in the course of the iteration. Unloading is regarded as non-physical behaviour and steps are often taken to reverse it in some way (Holt and Parsons 1979).

It was found necessary to introduce an extra parameter when reverse plastic straining was introduced. In this case, the timestepping is terminated when all plastic straining has finished, and this occurs when all stress states actually lie on the yield surface (rather than on or inside it). If the timestep is allowed to become increasingly large, oscillation will occur and the termination criterion may never be satisfied. The solution is to impose an upper limit on the timestep chosen by the timestepping algorithm (Owen and Hinton 1980, p.277). This maximum timestep is often not much bigger than the initial timestep but, paradoxically, decreasing the maximum can improve convergence. In fact, there is an optimum value of Δt_{max} for a given problem, to obtain the fastest convergence.

CHAPTER 5. RESULTS (1)

This chapter will illustrate the numerical accuracy of the method by applying it to problems with axial symmetry. These results were published in Reed (1987). The measures to prevent undershoot described above (§4.4) were not used in these analyses.

The axisymmetric tunnel problem may be defined as follows: a tunnel of circular cross-section, radius r_0, is excavated in an infinite rock mass which has a hydrostatic in situ stress field of magnitude q in all directions. Because of the axial symmetry, the problem may be analysed in one dimension. If it is assumed that σ_z remains the intermediate principal stress, and if an elastic-brittle plastic rock model is used, then there are analytic solutions for the tangential stress σ_θ and radial stress σ_r (which are the major and minor principal stresses respectively) using both the Mohr-Coulomb and the Hoek-Brown yield criteria. Reed (1986a,b) has proposed a one-dimensional finite element formulation which is able to use the Drucker-Prager flow rule, among others, to predict radial displacements as well as stresses.

The plastic region in the solution consists of an annulus around the tunnel, from the tunnel radius r_0 to an interface at r = R; outside this zone the rock remains elastic. For a brittle plastic rock the tangential stress is discontinuous across the interface, although the radial stress is continuous. The situation is sketched in fig.5.1. Analytic and numerical results are now summarised for two problems; one with a Mohr-Coulomb rock model, and the other using the Hoek-Brown model. In both cases the tunnel radius r_0 = 4 metres, and the elastic parameters were E = 20 GPa and v = 0.4.

(i) Mohr-Coulomb problem.

The material properties used were:

σ_c = 40 MPa, s = 1.0, s' = 0.25, k = k^1 =3

so that the drop in strength at yield was from 40 MPa to 20 MPa.

The in situ stress q = 40 MPa.

A finite element mesh of 18 elements was used, shown in fig.5.2, with only one quarter of the continuum being analysed. Infinite elements were used at the outer boundaries of the mesh. The axial symmetry of the mesh means that there are sets of six Gauss-points having the same radius, which should all have the same major and minor principal stresses; any random errors introduced in the algorithm by the evaluation of $\hat{D}$ will be shown up.

Five load increments were used, and the results are shown graphically in fig.5.3. Graph (a) shows the original (dashed line) and deformed (full line) mesh, using a distortion factor of 30. Graph (b) indicates the

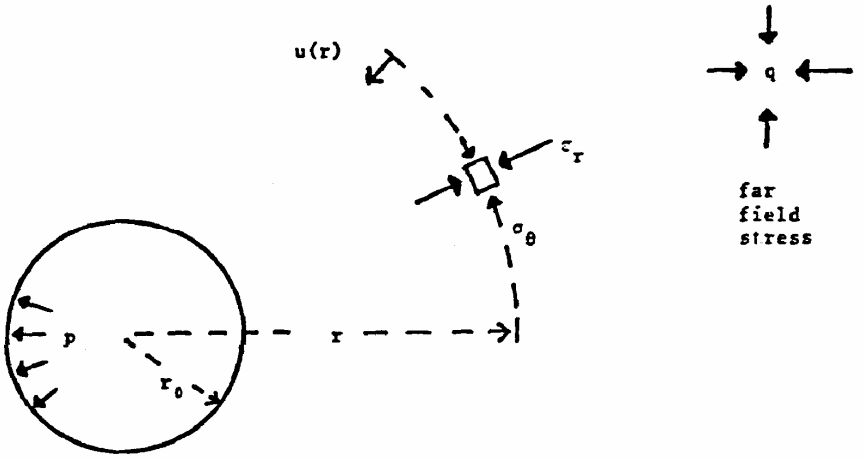

Tunnel wall

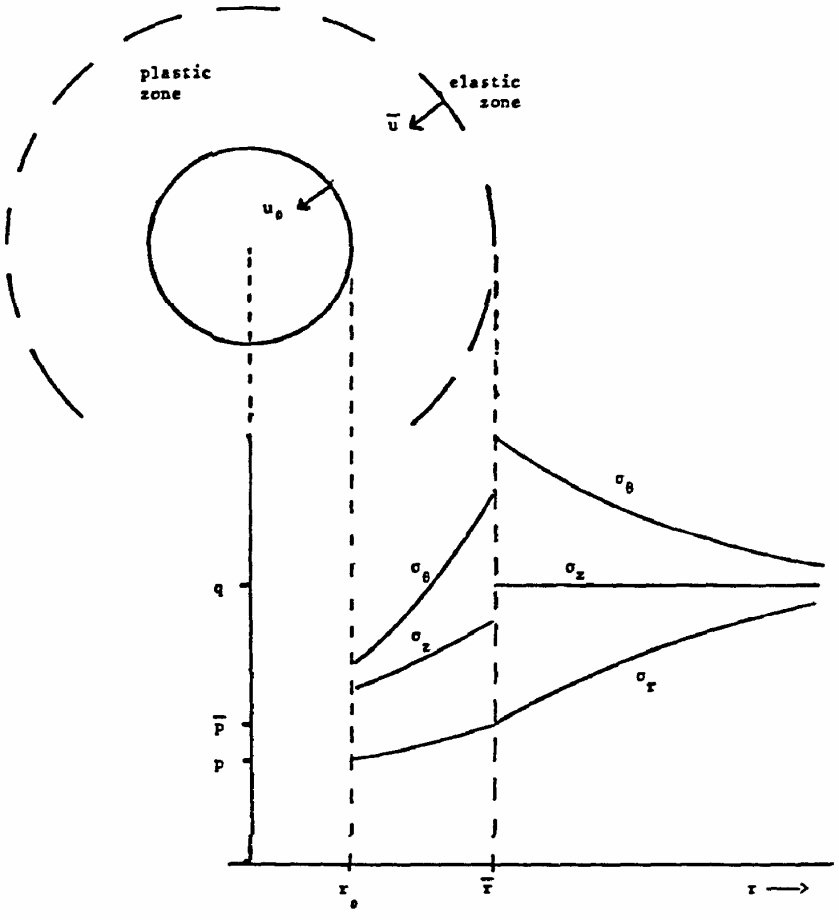

Fig. 5.1

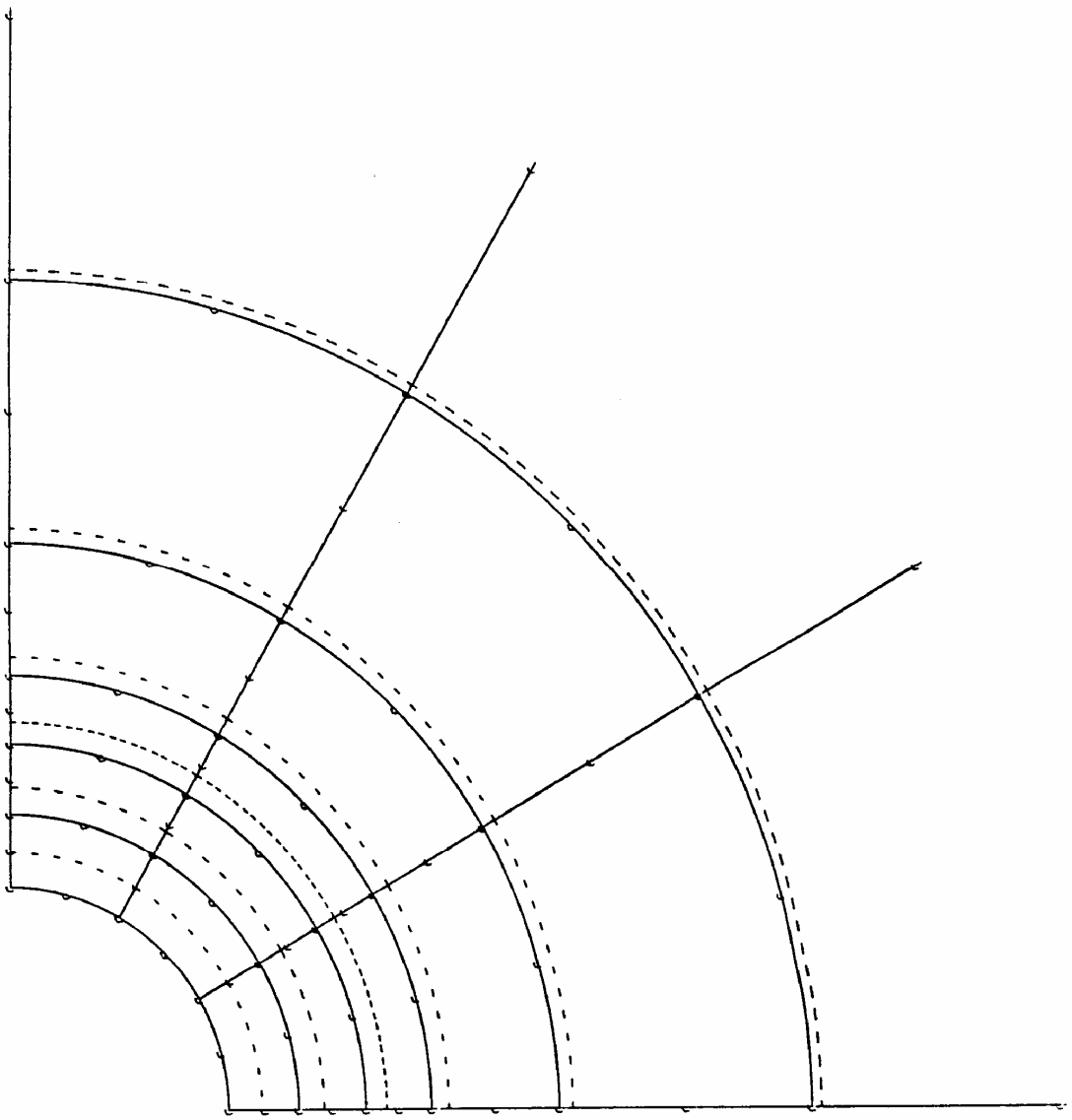

Fig. 5.2 (showing typical original and deformed meshes)

Fig. 5.3

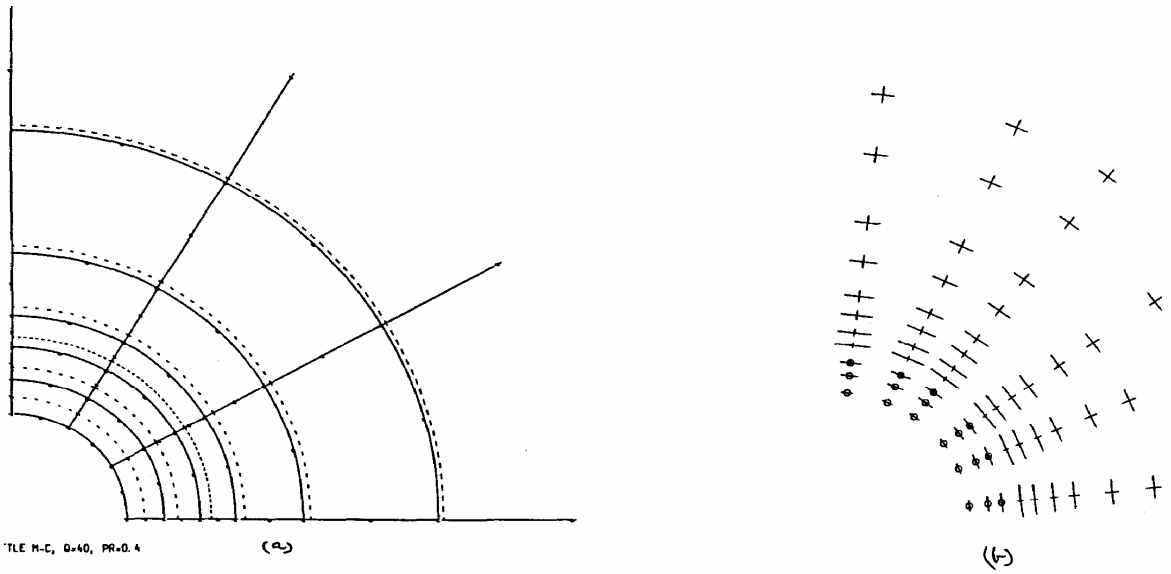
TLE M-C, D=40, PR=0.4
(a)
(b)

Fig. 5.4

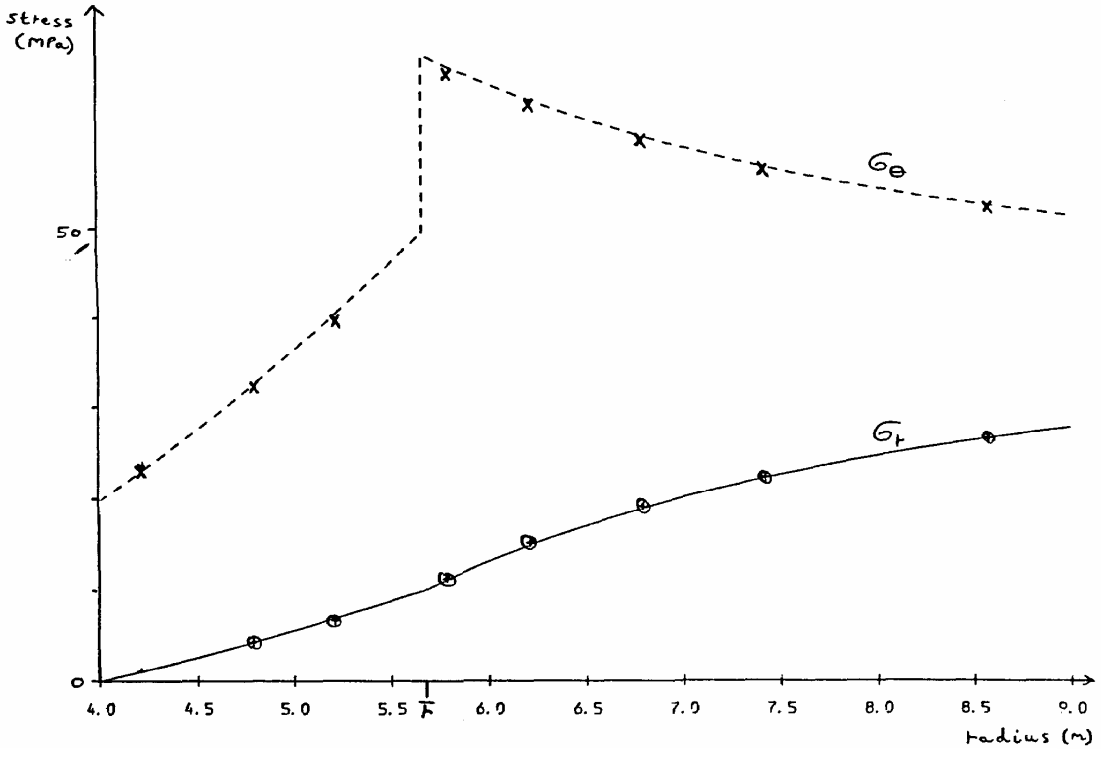
stress (MPa)
50
0
σ_θ
σ_r
4.0
4.5
5.0
5.5
6.0
6.5
7.0
7.5
8.0
8.5
9.0
radius (m)

Fig. 5.5

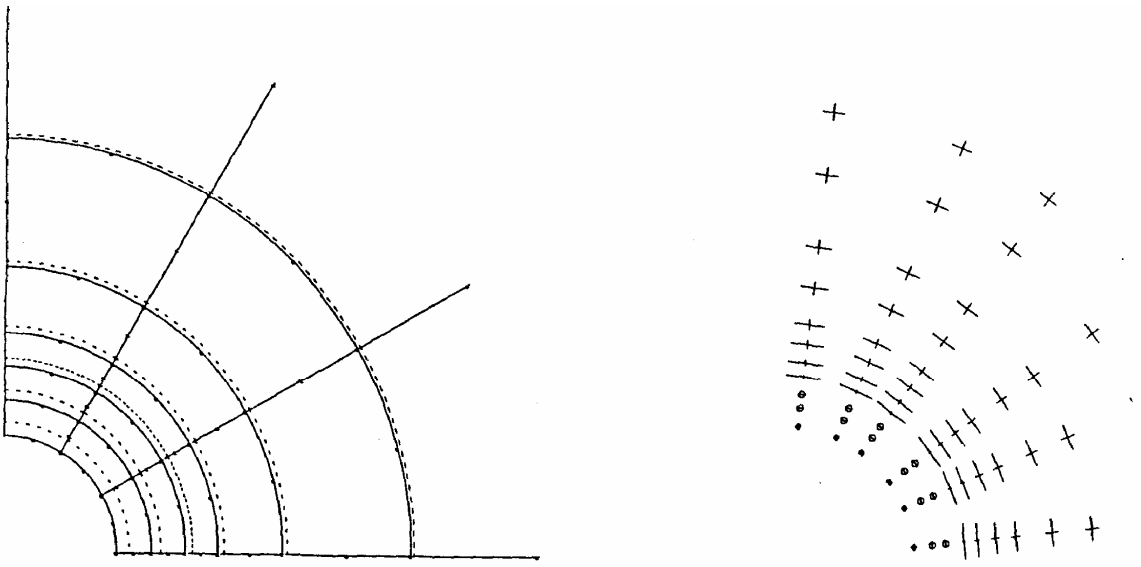

Fig. 5.6

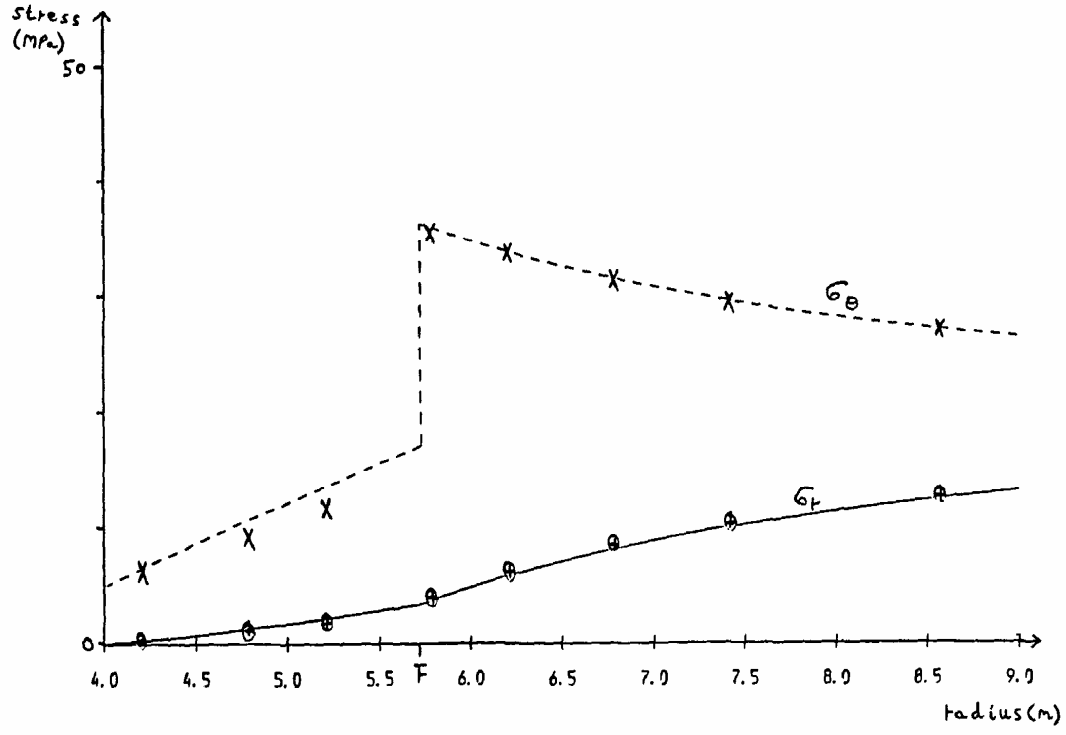
stress
(MPa)
50
0
σ_θ
σ_r
4.0
4.5
5.0
5.5
F
6.0
6.5
7.0
7.5
8.0
8.5
9.0
radius(m)

magnitude and direction of the major and minor principal stresses in the xy-plane; very good axial symmetry is obtained. Stresses are evaluated at the Gauss-points of each element; those points indicated by circles have yielded plastically during the deformation. Stresses at the same radius differed by less than 0.05%. Comparison with the analytic stress solution is made in fig.5.4, with stress plotted against radius; again there is excellent agreement,

(ii) Hoek-Brown problem.

The same problem geometry and element mesh were used, and the same elastic parameters. The plastic material parameters were:

$$\sigma_C = 50 \text{ MPa}, \; s = 0.1, \; s' = 0.01, \; m = 5, \; m' = 1,$$

so that the strength dropped from 15.8 MPa to 5 MPa on yield.

The in situ stress was q = 20 MPa.

Results from the finite element solution, in which the load was added in six increments, are shown in fig.5.5. Excellent axial symmetry is again obtained. The principal stresses are compared with the analytic solution in fig. 5.6. Here it is seen that there is a small overshoot in the stress reduction for yielded Gauss-points. This is due to the high curvature of the failure surface; more accurate results would be obtained by using a smaller value of the fluidity parameter y. The minor principal stresses at Gauss-points closest to the tunnel wall have become negative during the deformation, and the 'no-tension' criterion brought into play.

In both problems the predicted displacements can be compared with the solutions from a one-dimensional finite element analysis using a much finer mesh (with 16 quadratic elements between r = 4m and r = 6m) . In the Mohr-Coulomb problem, this one-dimensional analysis gave a tunnel wall displacement of 17.907mm radially inwards, whereas FESTER predicted an inward movement of 17.795mm. In the Hoek-Brown problem, the inward movements of the wall were 13.661mm and 13.519mm respectively. This is excellent agreement considering that such a coarse mesh was used in FESTER.

In the following results, the axisvmmetric finite element mesh was retained, but the rock was orthotropic, with Young's moduli of 15 GPa in the horizontal direction and 10 GPa vertically, a shear modulus G = 7 GPa and Poisson's ratio v = 0.3. The in situ stress field was also made non-hydrostatic: the vertical in situ stress c_v = 36 GPa, but the horizontal stress made greater or less, with lateral stress ratio K_0 = 0.6 (giving σ_h = 21.6 MPa) or K_0 = 1.4 (σ_h = 50.4 MPa). The rock was a brittle Mohr-Coulomb material, with the plasticity parameters of the previous section.

Figure 5.7 shows displacement and stress plots when K_0 = 0.6. Plastic yield has occurred at the sides of the tunnel, and the tunnel profile has

assumed a squarer shape (displacements of the deformed mesh have been exaggerated by a factor of 40 in fig.5.7 et seq.); the increased inward movement of the tunnel side is caused by the plastic yield, and that of the tunnel roof is a consequence of the elastic orthotropy.

A horizontal plane of weakness was now introduced in the rock, with cohesion C_j = 7 MPa and angle of friction $\psi_j = 30^0$. (This is equivalent to a triaxial stress factor k^j = 3 and unconfined compressive strength σ_j = 24.2 MPa). Some sliding along the jointing plane occurred at the tunnel wall above the yield zone, but otherwise the results for stresses and displacements were little changed.

Rather more interesting are the results when K_0 = 1.4. For the case of a homogeneous orthotropic rock (fig.5.8), a broad plastic zone is created across the tunnel roof. When the horizontal plane of weakness is introduced (fig.5.9), joint sliding occurs in a long narrow zone penetrating into the rock at about 60° to the horizontal; these Gauss points are indicated by a star in fig. 5.9, This has the effect of reducing the depth of the yield zone, so that plastic yield is now concentrated more narrowly at the crown of the tunnel roof. The deformed tunnel profile is also significantly changed, with inward movement concentrated at the tunnel crown.

To analyse practical problems, with a more complicated geometry and using a finer mesh, a pre-processor package is desirable. This will enable the user to input the mesh interactively, refine it, and display mesh and results graphically. Such a pre-processor has been developed for FESTER, and its theoretical aspects will be discussed in the next chapter.

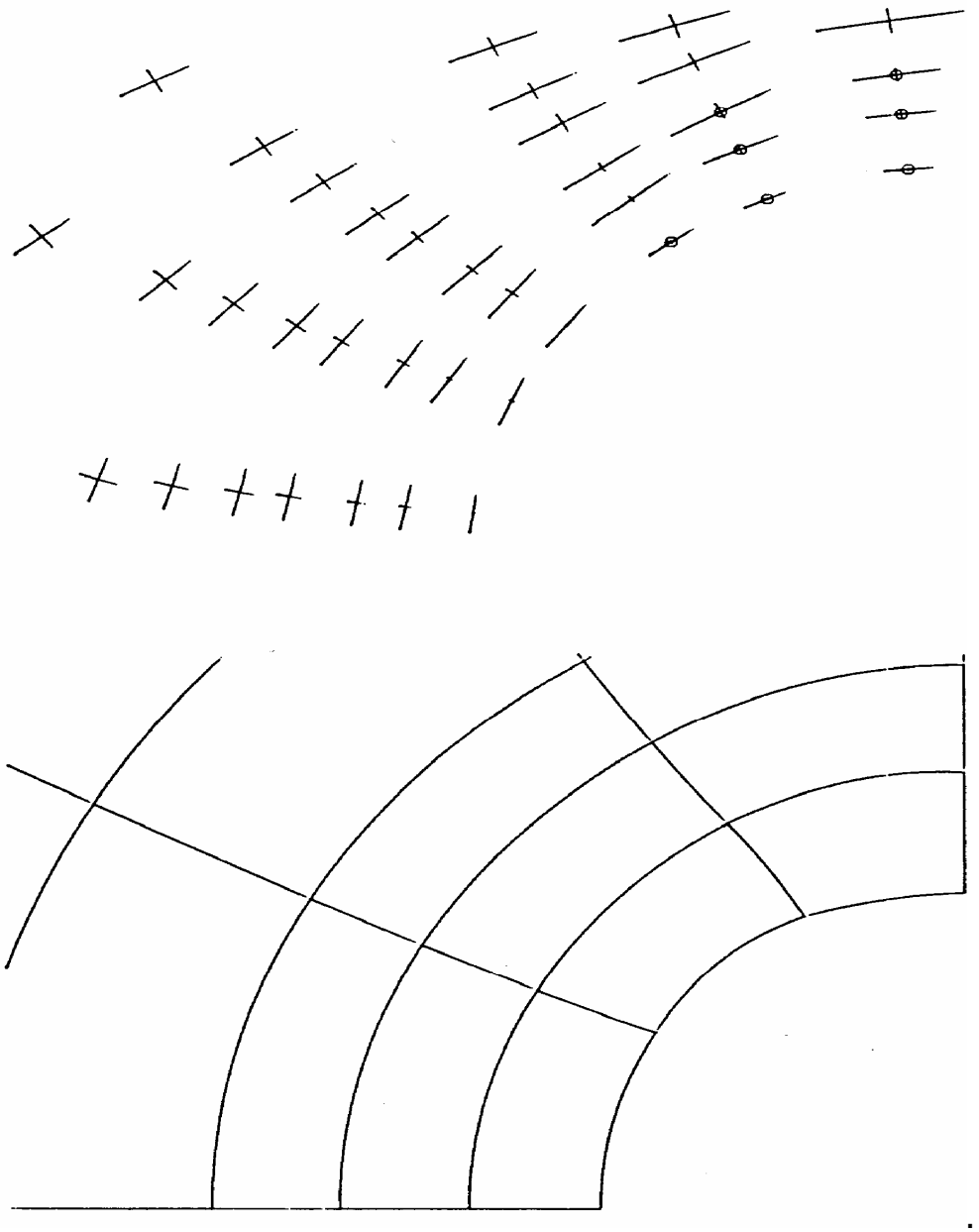

Fig. 5.7

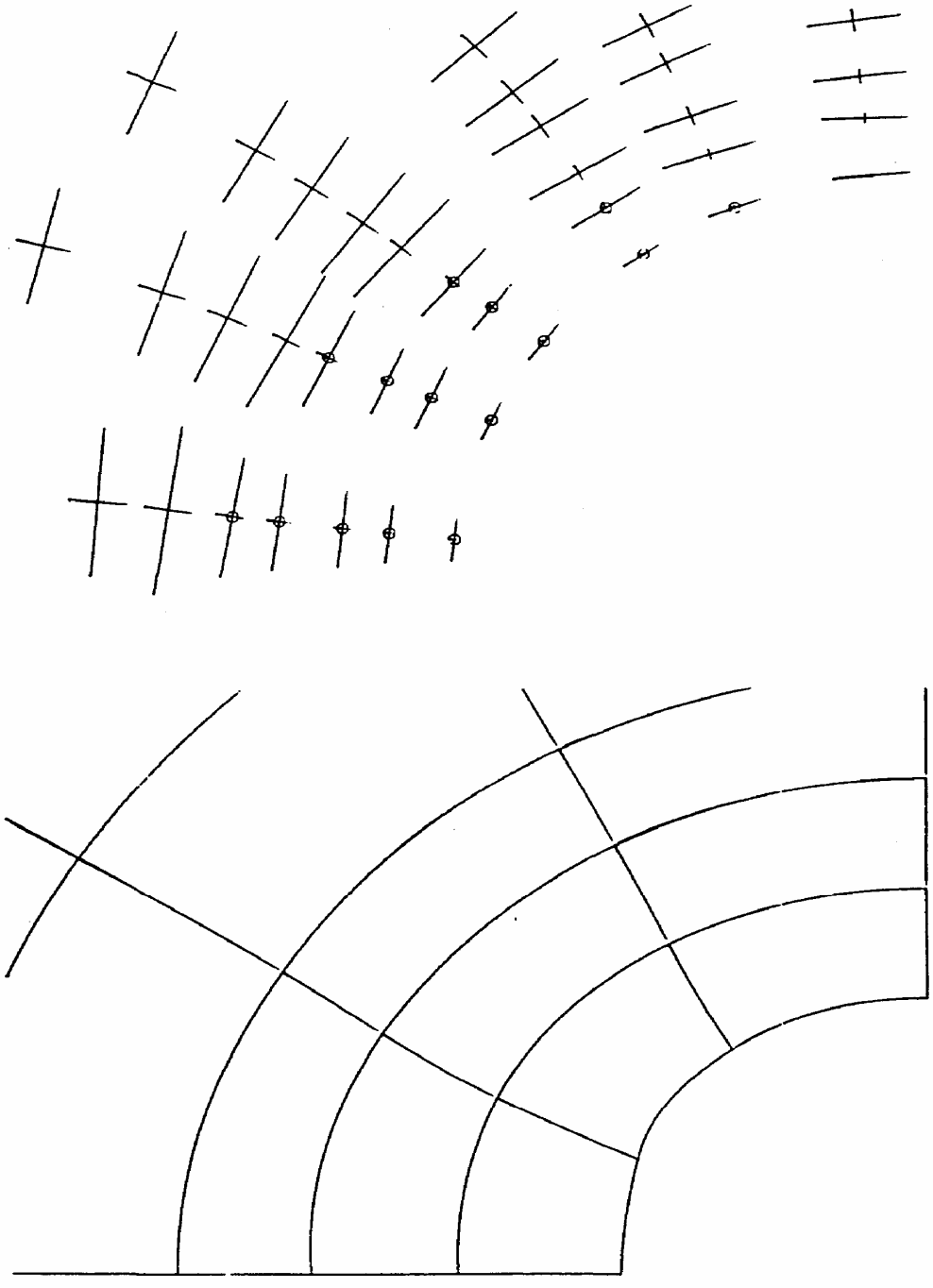

Fig. 5.8

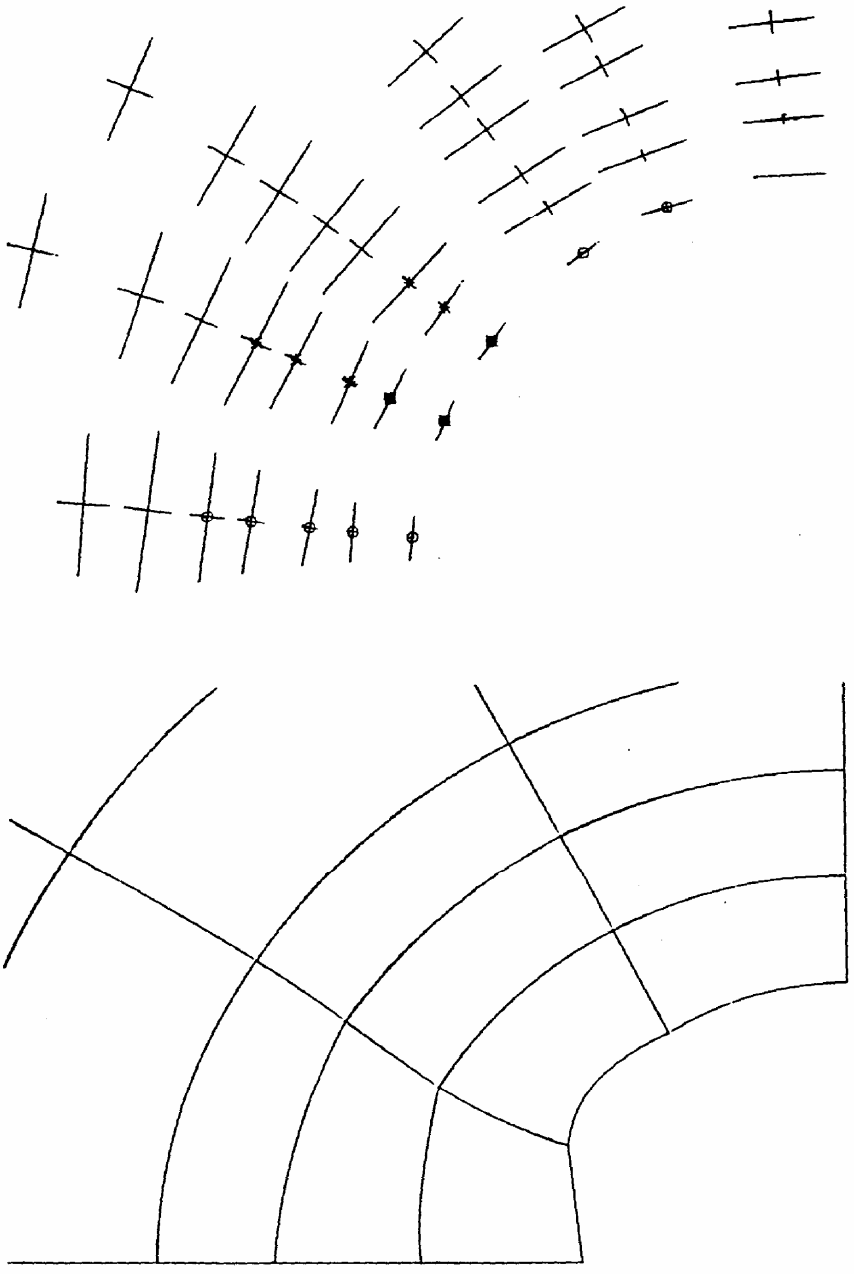

Fig. 5.9

CHAPTER 6. PREPROCESSOR

The data file for a finite element package can often be very tedious to prepare and check. To overcome this problem a preprocessor is often available to lighten the work of preparing lists of elements and nodes. A small preprocessing package (PREFES) has been written specially for the FESTER package which guides a user through mesh preparation and which controls the details that make the information recognisable by FESTER.

The preprocessor is based on a data file which it builds up itself from information given to it by the user. This file does not have to be complete for the preprocessor to be able to read it. Most of the package is concerned with requesting information from the user, checking that it makes sense, and putting it in the correct slot in the data file. The important parts of the package are the routines which refine a mesh and reduce frontwidth, and the ideas behind what they do is described below. A final routine performs the task of writing a file suitable for input to FESTER itself. To aid the user in checking the mesh and interpreting the results there are also graphics programs to draw the mesh and display displacements and stresses. Full user instructions are given in the Appendix.

6.1 Refinements

The refinement of a finite element mesh may be carried out by subdividing the elements into smaller but similar elements. Thus, the basic shape of the final mesh can be modelled using as few elements as possible and then a more detailed mesh can be created from this by mesh refinement. The original coarse mesh is usually constructed from 8-node quadrilateral elements which allow for curved boundaries to be modelled and are easy to use. In the discussion here, the new refined elements will also be 8-node quadrilaterals. Modifications of the discussion below allow for the possiblity of other types of element, in particular the 5-node infinite element and the 6-node joint element.

Let S be the standard square element

$$S = \{(\xi, \eta) : -1 \le \xi \le 1, \quad -1 \le \eta \le 1\}$$

and suppose that S is mapped to the 8-node quadrilateral element S' by the transformation

$$X = \sum_{i=1}^{8} N_i(\xi,\eta)\, X_i \qquad (6.1.1)$$

$$Y = \sum_{i=1}^{8} N_i(\xi,\eta)\, Y_i$$

where (x_i,y_i) are the coordinates of the nodes of S^1 and N_i are the standard shape functions (2.2.1) for a 8-node quadrilateral. Let V_1, i = 1,..,n and W_i, i = 1,..,m be indexed collections of real numbers and define

$$\xi_i = -1 + \frac{2}{V}\sum_{k=1}^{i} V_k, \qquad i = 0,.....,n$$

$$\eta_i = -1 + \frac{2}{W}\sum_{k=1}^{i} W_k, \qquad i = 0,....m$$

and

$$\xi_i + \frac{1}{2} = \xi_i + V_i / v, \qquad i = 0,....n-1$$

$$\eta_{i+}\frac{1}{2} = \eta_i + W_i / W, \qquad i = 0,....m-1$$

Where

$$V = \sum_{k=1}^{n} V_k$$

And

$$w = \sum_{k=1}^{m} W_k$$

The new element boundaries are given by mapping the lines $\xi = \xi_i, i = 0,....,n$ and $\eta = \eta_i, i = 0,...,m$ using (6.1.1.).The nodes of the new elements are given by mapping the points $(\xi_i, \eta j)$ for i=l,…..n and j=1,…..m and the points $((\xi_i + \frac{1}{2}, \eta j))$ and $(\xi_i, nj + \frac{1}{2},)$ for i=0,..n-l and j=0,..m-l.

The numbering of the nodes of the refined mesh is done for the whole mesh and not for individual elements as is often the case in similar mesh refining algorithms. The usual method is to number the new nodes element by element in the original mesh and then to coalesce nodes on the boundaries between two elements where the same node has been assigned two node numbers. This is done by comparing the coordinates of all pairs of nodes and assuming that nodes with the same coordinates are in fact the same single node. This is usually satisfactory, but a preprocessor for FESTER must be able to cope with joint elements where opposite nodes in the element have the same coordinates.

The method used here is to decompose the original mesh into three sets E_0, E_1, and E_2,..E_0 contains all the points that are corner nodes, E_1 contains the edges and E_2 contains the elements. Any new nodes, generated as above, in the interiors of members of E_0, E_1, and E_2 can now be numbered, and each new node receives a unique number. For each old element, the numbers of the new nodes on the boundary can be obtained from the numberings of the members of E, which make up the boundary, and likewise the numbers of nodes at the ends of each member of E, can be obtained from the numbering of the corresponding members of E_2.

6.2 Frontwidth reduction

The finite element method requires the inversion of a stiffness matrix. In methods for non-linear problems, such as that used in FESTER, a stiffness matrix may need to be inverted many times in order to solve a problem to a given accuracy. The matrix inversion method on FESTER is of a frontal type where the variables are eliminated in an order governed by the construction of the mesh. The number of operations required to invert a given matrix is bounded by the number required by a typical band solver. Another (better) bound is given as a function of the maximum frontwidth (Sloan and Randolph, 1983), where the frontwidth is the number of equations being used at any particular stage by a frontal solver. Fill-in during elimination still occurs when a frontal method is" used, but it is, in general, less than with a band solver. The number of operations required at each elimination grows as the square of the frontwidth at that stage (Sloan and Randolph, 1983). Taking these comments together, it can be seen that it is desirable to reduce the bandwidth and maximum frontwidth of the stiffness matrix before it is inverted and also that it is desirable to keep the average frontwidth as low as possible. Bandwidth reduction of a matrix may be carried out simply by reordering the varibles. Unfortunately, the problem of finding an optimal reordering seems to be hard (in the computational sense) since there does not exist either a simple way to characterize an optimum reordering or an efficient algorithm for finding such an order. Hence the methods that have been proposed have not been proved to be optimal and indeed it is usually possible to describe a simple example which results in a very bad ordering of the unknowns. The methods are justified by hand-waving argument and by trying them on a range of problems and comparing the results with other methods.

Many methods have been proposed, but a review of them will not be attempted here since there are many already published (see, for example, Sloan and Randolph, 1983). Only the method used will be described. The

method is due to Sloan (1986) and it incorporates several features to reduce the amount of work and storage required compared with earlier algorithms. In the next section the machinery from graph theory that will be needed in the discussion will be described and then the algorithm itself will be demonstrated.

6.2.1 Graph concepts

The concepts required by the algorithm may be expressed entirely in terms of the dispositions of elements of a matrix, but it is traditional in this field (and more lucid) to use concepts from graph theory. A graph G can be defined as a pair <V,E>, where V(G) is a set of objects called vertices and E{G) is a set of unordered pairs of members of V. In other words a graph here will be simple, undirected and without loops. The following nomenclature will be useful. Two vertices u,v are said to be adjacent if (u,v) E, and the degree of a vertex, $\delta(V)$ is the number of vertices which are adjacent to v. A path in a graph is a sequence of vertices $v,V_2v_3v_4....v_n$ where, each pair $\{vi,v_i+,\}$ ε E, and its length is number of such pairs it contains (i.e. n-1 in this case). The distance between two vertices is the length of the shortest path containing both of them. A shortest path between two vertices a maximal distance apart is called a diameter of the graph, and its length is also called the diameter of the graph.

A numbering of a graph with n vertices is a one-to-one function f: $V \rightarrow \{1,2,...,n\}$. The bandwidth of the graph relative to a numbering f, β_f is defined as

$$\beta_f = \max_{V,u \in V} \{|f(V) - f(u)|\}$$

Now we relate these concepts to matrices. For any symmetric nxn matrix K=(kij) graph (called the adjacency graph) may be constructed by letting $V = \{v, v_2,...,v_n\}$ and $E = \{\{Vi,V_j\}: k_{ij} <>0 \text{ and } i <> j\}$. Note that a numbering of the adjacency graph of a stiffness matrix corresponds to an ordering of the unknowns and that the bandwidth of the graph is precisely the bandwidth of the matrix relative to that ordering.

A useful concept for bandwidth reduction is that of a level structure. The level structure L(S) rooted at a subset S of V is a partition of V into subsets $1, ,1_2 ,. . . ,1_h$ where

(i) $1, = S$

(ii) All vertices adjacent to vertices in 1_i (i<i<h) are in 1_{i-1}, 1_i or $1_{i+1.}$

(iii) All vertices adjacent to vertices in 1_h are in 1_{h-1} or $1_{h.}$

It can be seen that all the vertices in level i are at a distance of i-1 from S. h is called the height of the level structure, $w_i = |1_i|$ is the width of level i and max $\{w_i\}$ is the width of the level structure.

6.2.2 The algorithm

The algorithm for frontwidth reduction proceeds by constructing the graph of the matrix as described above and then finds a numbering of the vertices which is hoped to have a smaller bandwidth. The algorithm needs a vertex to start from; the method of finding a good starting vertex is described first and then the actual renumbering method is discussed.

The graph to which the algorithms are applied is constructed directly from the mesh information. Without loss of generality it is assumed that each node represents one degree of freedom, since there will be an entry in the stiffness matrix corresponding to nodes i and j if and only if they are in the same element and it does not matter how many degrees of freedom each node has. Hence each vertex in the adjacency graph constructed from a mesh will correspond to a node in that mesh, and each edge to each pair of nodes that are in the same element. For example, the graph corresponding to a mesh of linear triangles is isomorphic to the grid of edges of the mesh itself.

Observations by other authors (for example, Gibbs et al., 1976) suggest that it is good to start renumbering from what they term a pseudo-peripheral vertex. These are vertices that are almost a maximal distance apart - i.e. the distance between them is close to the diameter of the graph. The definition of such vertices seems to be "those vertices that are found using the following algorithm", and an algorithm is then presented. An algorithm suggested by Gibbs et al is as follows.

1. Pick any vertex of minimal degree.
2. Generate the level structure $L(v) = \{1,,...,1_h\}$
3. Take each $u \in 1_h$ in order of degree and generate the level structure L(u). If, for some u, L(u) has greater height then L(v) then v:=u and go to step 2.
4. Let $u \in 1_h$ be the vertex for which L(u) is the least. The algorithm finishes with u,v pseudo-peripheral vertices.

The algorithm used here is the one suggested by Sloan(1986) and is the same as the above but with 2 modifications, both in step 3. Once the vertices in l_h have been sorted in increasing order of degree, then the Sloan method only generates level structures for the first (m+2)/2 members of 1_h, where $m=|1_h|$. The other change is to keep a record of the minimum width of level

structure found and only to return to step 2 if the higher level structure also has a width less than the minimum already found.

6.2.3 Labelling

Once two pseudo-peripheral vertices have been found, they can be used to start the relabelling algorithm. In order to describe this algorithm, we need a few terms. Suppose that at some stage in the process of relabelling, $S \subseteq V$ is the set of vertices that have already received a label, and let $L(S) = \{1_1, 1_2, \ldots, 1_h\}$ be the level structure rooted on S. Then if $v \in 1$, (= S), it is termed postactive, if $v \in 1_2$ it is termed active, if $v \in 1_3$ it is preactive, otherwise v is called inactive. The current degree of a vertex is a measure of the increase in the number of active vertices if it were to be labelled. It is defined as

$$n_V = (d(V) - C_V) + K_V$$

where C_V is the number of vertices adjacent to v which are either active or postactive, and

$$k_V = 0,1$$

The algorithm assigns a priority to each vertex. This is a weighted sum of its current degree and its distance from the end vertex. Initially, one of the pseudo-peripheral vertices is given preactive status. The algorithm continues by labelling an active or preactive vertex which has the highest priority (which then becomes postactive), and then updating the priority and status of each vertex taking this change into account. The priority is calculated to ensure that vertices with low current degree and which are far from the end vertex have a high value. This ensures that the increase in the number of active vertices is small (a local condition) and that the global structure of the graph is taken into account by labelling vertices far from the end vertex before those closer. The weights used to calculate the priority can be changed, but here we use those recommended by Sloan (1986).

Once the nodes have been relabelled the elements are relabelled to reduce the frontwidth and the actual node renumbering is discarded. Sloan (1986) renumbers the elements in the order of the lowest numbered nodes in each element and this is what is done here. For each node a list of the elements containing that node is made. Then the nodes are checked one by one in order, and if there is any element containing the node which has not received a number, it is given one. This continues until all the elements have been renumbered.

CHAPTER 7. RESULTS (2)

A series of trial runs has been carried out in which the mesh was kept the same and the material properties varied. The trials were conducted to test the various models that are included in the program on a realistic mesh and in more realistic and complex combinations. The trials have also enabled some experience to be gained as to the choice of the solution parameters and also some adjustments have been made to the numerical techniques to improve the solutions. The example mesh was of an arched tunnel with a circular roof and straight sides and floor. The mesh is shown in fig. 7.1.

The main problem encountered during the trials was undershoot. The viscoplastic constitutive law requires that plastic straining only occurs when the stress value lies outside the yield surface. When this was implemented strictly in the algorithm it was found that, for the mesh in fig. 7.1, the stress values at several yielded Gauss points finished well inside the yield surface at the end of the solution. This behaviour is what is refered to as undershoot. In the case at hand, the first solution to the problem of undershoot was to assume that it was due to the approximations in the implicit viscoplastic algorithm. However, attempts to improve accuracy showed that undershoot proved to be very persistent. Indeed, even trial runs with fixed small timesteps suffered from undershoot. The approach eventually adopted was to allow reverse plastic straining at Gauss points that undershoot - see section 4.4.

The trials have suggested how the values of the various solution parameters affect the quality of the solution and the number of time steps needed to obtain convergence. It was found that quite small values of the time step control parameter τ were usually necessary. Good values for this mesh seem to be between about 0.1 and 0.3. Larger values lead to a decrease in accuracy and lowering of the rate of convergence and smaller values are too restrictive, greatly increasing the number of time steps required. The maximum magnification factor for increasing time steps was kept at 1.5 since any larger value was found unsatisfactory. The fluidity parameter in the flow rule γ was in most cases fixed at 0.01. With this value of γ the initial timestep was usually taken as 0.01. The parameter θ was fixed at 2/3.

Several examples have been chosen here to illustrate the various capabilities of the program. The various sets of material properties that were used are listed in full in table 7.1. As can be seen the values do not vary much between the materials, but any unsual values have been picked out

in a different type face. All materials had a Mohr-Coulomb yield surface. A summary of the examples that are to be discussed is given in table 7.2. This table gives the material that was used in the mesh, τ the time step control parameter, the initial and maximum allowed timesteps, the convergence tolerance and the number of timesteps required to attain convergence. The convergence tolerance is expressed as a percentage. At the end of each time step, the effective visco-plastic strain rates are calculated and summed. Times stepping ceases when this sum is less than TOLER% of its initial value.

All the trials assumed a uniform hydrostatic stress field is present initially, and that the tunnel is at a depth of 500 metres. The increase in load with depth was taken to be 0.025 MPa per metre, giving an initial uniform stress field of 12.5 MPa.

The tunnel represented by the mesh is supposed to have a circular ceiling with a radius of 2 metres, and the side wall is 1 metre high.

Example 1 is the 'standard' example that has been used to test the program. Figure 7.2 shows a plot of the distorted mesh and of the principal stresses at the Gauss points. The small circles at some of the Gauss points denote the points that have yielded. The pricipal stress plot reveals that there is a discontinuity in the stress component parallel to the ceiling and side wall, and that the stresses parallel to the floor have become tensile.

Figure 7.3 shows similar plots for example 2. The material here yields more easily because of a lower triaxial stress factor. Hence more points have yielded, especially around the corner where the side wall meets the floor. This has changed the distribution of the resulting displacements, notably in the floor, but not their magnitudes (the centre of the floor has risen by about the same amount as in example 1). Example 3 has a smaller residual yield surface than example 1. This can be clearly seen as smaller principal stresses at yielded points in fig. 7.4. The displacements are larger all round the tunnel in this case and the more pronounced bulge in the side wall seems to be caused by the increase in yielded points in that region. Example 4 is not illustrated because it has no striking new features. The interest in this example lies in the solution. This example used a different value of the dilation parameter α in the flow rule. Table 7.2 shows that it was possible to use a much larger maximum time step than in the other examples, and that it required relatively few time steps to achieve convergence to the given tolerance.

The next example (number 5) is of an anisotropic material. The solution obtained by FESTER does not seem much different to example 1. The

displacements can be seen to be smaller (fig- 7.5), but the distorted shape of the tunnel is not very different. The yielded points were in the same positions. However, more time steps were required to achieve convergence and the solution parameters had to be adjusted to improve the speed of convergence (see table 7.2). A small value (0.01) of the maximum time step was used in this particular example.

Example 6 uses the model for laminated material. In this material, the mass yield strength of the rock has been set high to deter this yield mechanism. Figure 7.6 shows the results obtained with this material. Points at which slippage of the laminations has occurred are marked by a star. The strength of this material σ_c has been made large to preclude any other yielding than the slippage of the laminations. The pattern of yielded points is very different to those in the previous examples. The yielded region at 45° in the ceiling is similar in orientation to yielding found in an axisymmetric tunnel with horizontal laminations. The displacements around the tunnel show large deformation occurring in the straight sides next to the corner, and this is associated with lines of yielded points deep into the rock emanating from the corner. It can also be seen that the ceiling has become distorted, with larger displacements in the 45° direction where the yielding has occurred.

The final example combines materials from two previous examples, material 1 being confined to a layer through the middle of the mesh, and material 6 making up the rest of the mesh. The mesh had to be slightly modified to make this realistic and the situation is illustrated in fig. 7.7. The pattern of yielded points and tunnel wall displacements are shown in fig. 7.8. The stars represent the slipping of the laminations, the circles failure of the rock, and the triangles show points at which the stress has exceeded the maximum tensile stress. The pattern of points in the laminated material is only slightly disturbed, but the pattern in material 1 is very different from that shown in fig. 7.2, since more points in the floor have yielded. The displacements show a further distortion of the ceiling compared with the laminated material on its own (fig. 7.6), and a distortion can be seen below the floor where the two materials meet. In this mesh there is no interface between materials and it would be more realistic to use joint elements between strata. This would alter the displacements in that part of the mesh.

Constant	Material number 1	2	3	4	5	6
E (GPa)	10	10	10	10	***20***	10
N	0.25	0.25	0.25	0.25	0.25	0.25
E_2(GPa)	-	-	-	-	10	10
ν_2	-	-	-	-	0.25	0.25
G (GPa)	-	-	-	-	2	2
β (○)	-	-	-	-	0	0
σ_C (MPa)	18	18	18	18	18	***40***
K	3.2	***2.8***	3.2	3.2	3.2	3.2
S	1	1	1	1	1	1
A	0	0	0	***0.1***	0	0
k'	3.2	***2.8***	3.2	3.2	3.2	3.2
s'	0.25	0.25	***0.09***	0.25	0.25	0.25
Γ	0.01	0.01	0.01	0.01	0.01	0.01
φ_j (radians)	-	-	-	-	-	0.524
c_j (MPa)	-	-	-	-	-	3
ψ_j	-	-	-	-	-	0
γ_j	-	-	-	-	-	0.01
σten (MPa)	5	5	5	5	5	5
σ'ten (MPa)	3	3	3	3	3	3

Table 7.1. Material constants for the materials used in the examples.

	Example number 1	2	3	4	5	6	7
Material	1	2	3	4	5	6	1,6*
T	0.2	0.2	0.2	0.2	0.2	0.2	0.2
Initial time step	0.01	0.01	0.01	0.01	**0.005**	0.01	0.01
Maximum Time step	0.015	0.015	0.015	**0.05**	***0.01***	***0.11***	0.015
TOLER	0.1	0.1	0.1	0.1	0.1	***1.0***	***1.0***
Number of Time steps	22	30	48	21	37	37	44

*In the laminated material (6) the joint fluidity γ_j had a value of 0.02

Table 7.2. Some parameters and results for the examples.

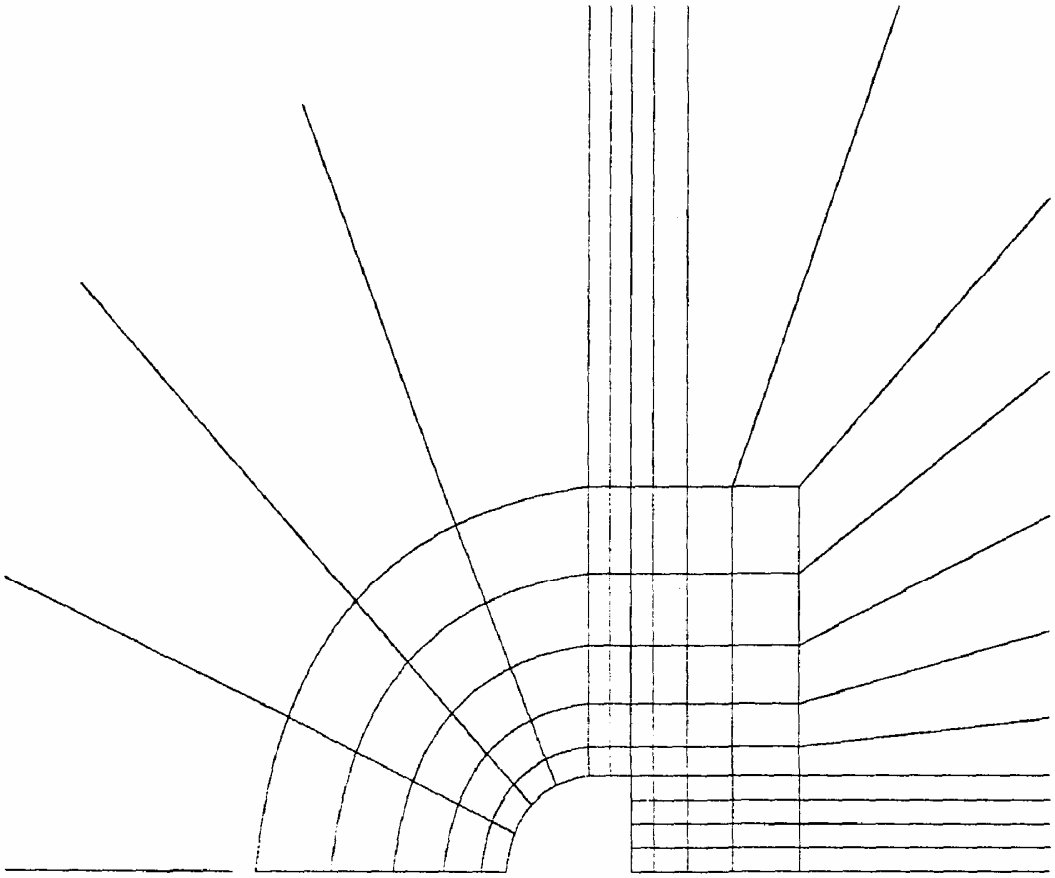

fig . 7.1

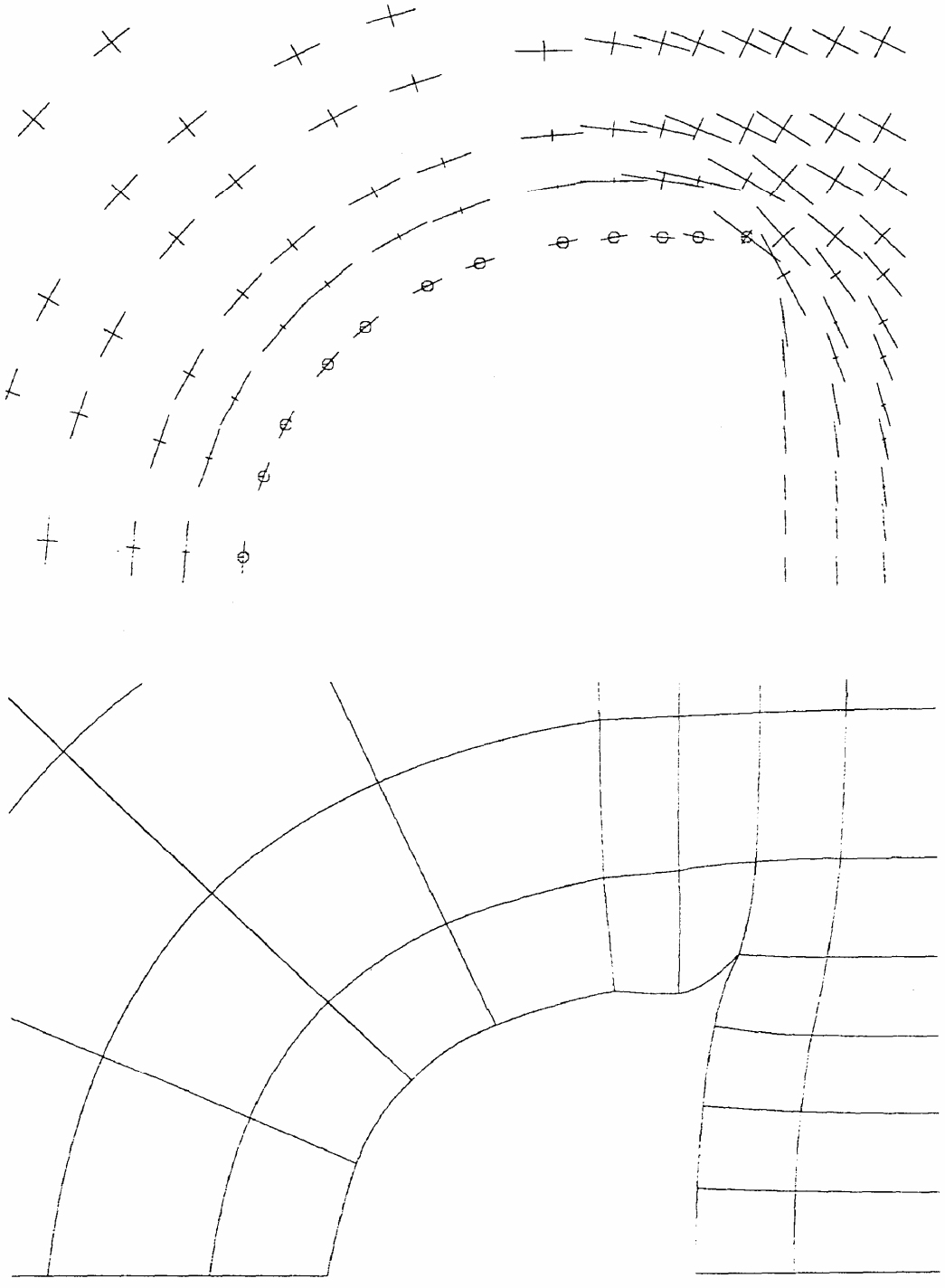

fig. 7.2

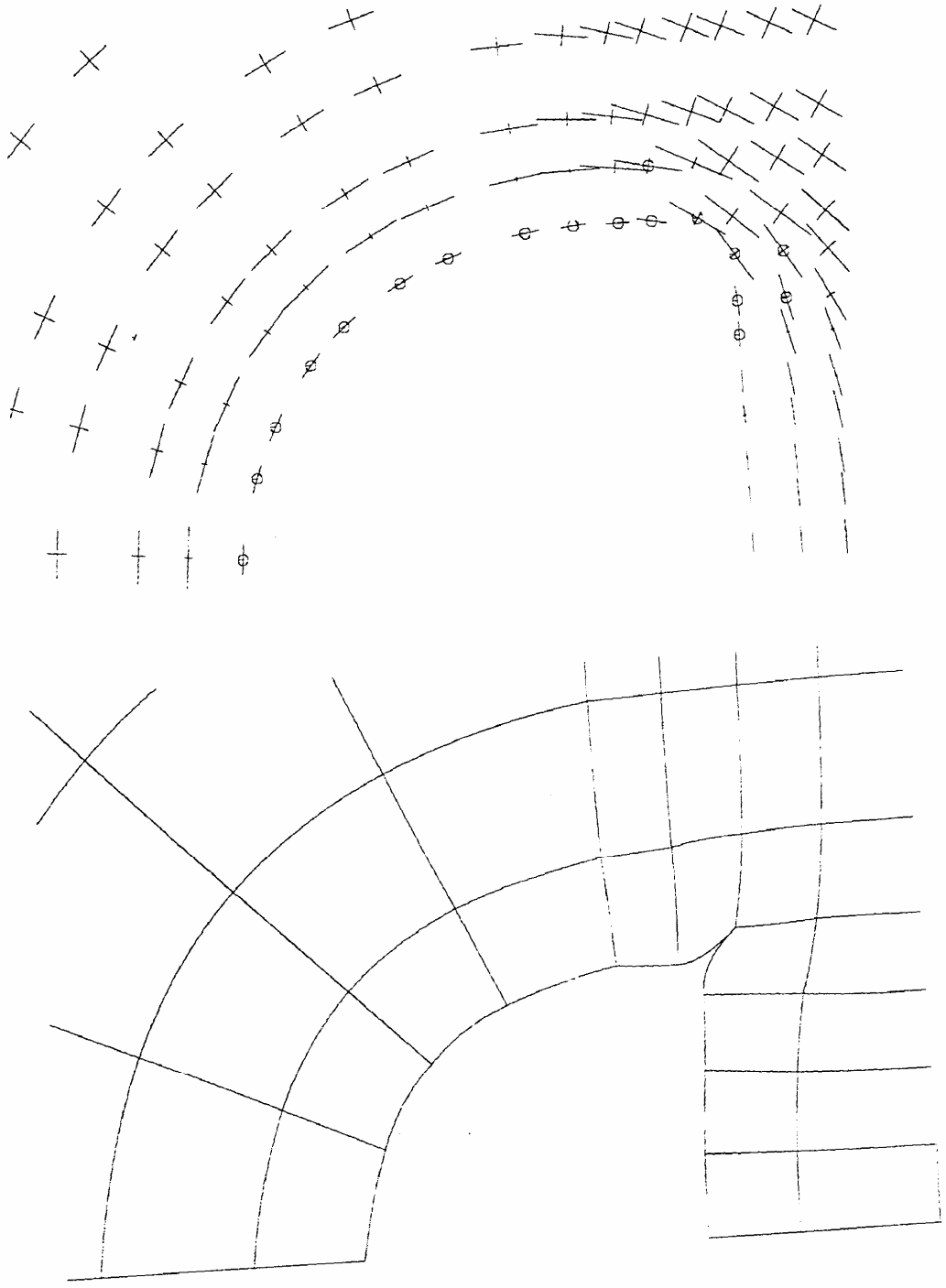

fig. 7.3

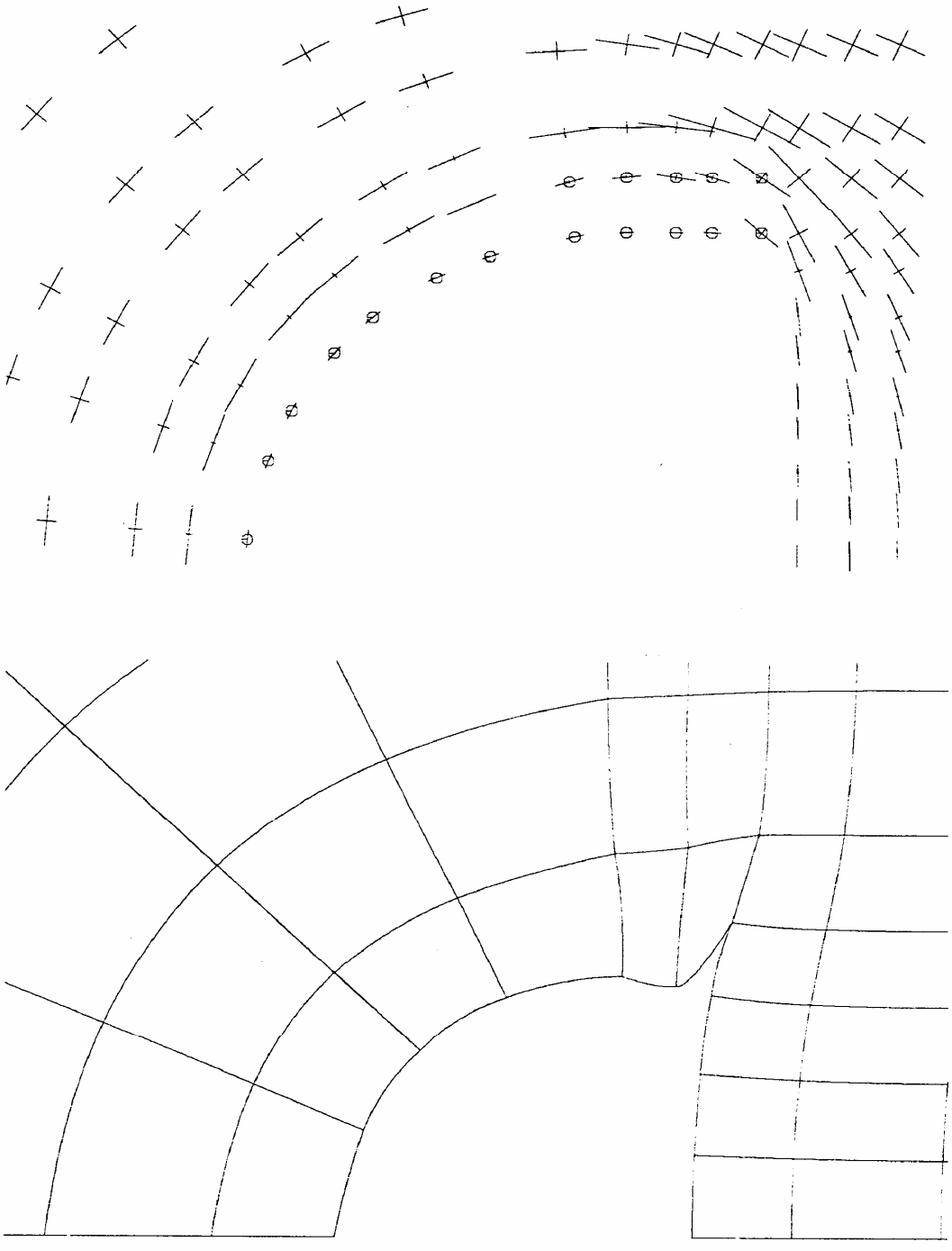

fig. 7.4

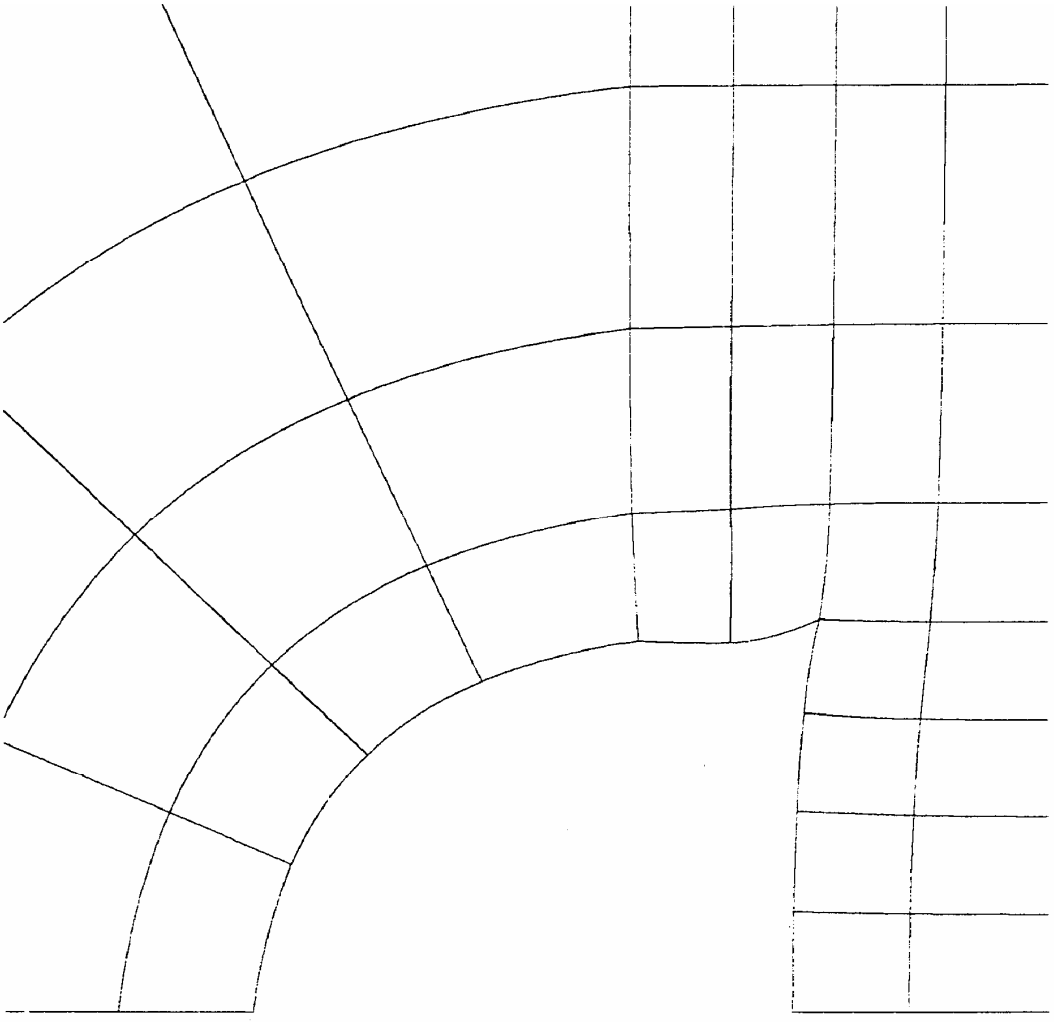

Fig. 7.5

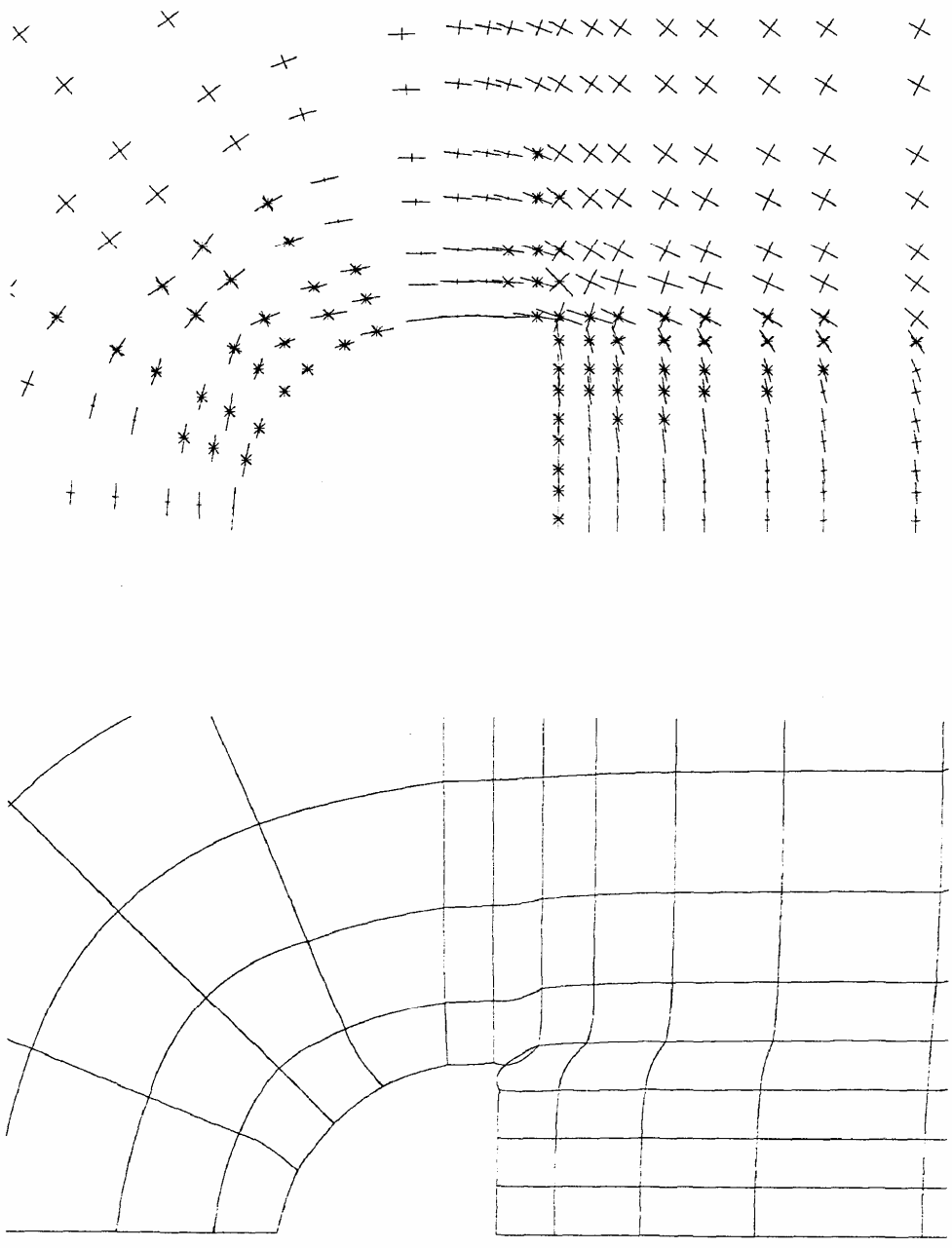

Fig. 7.6

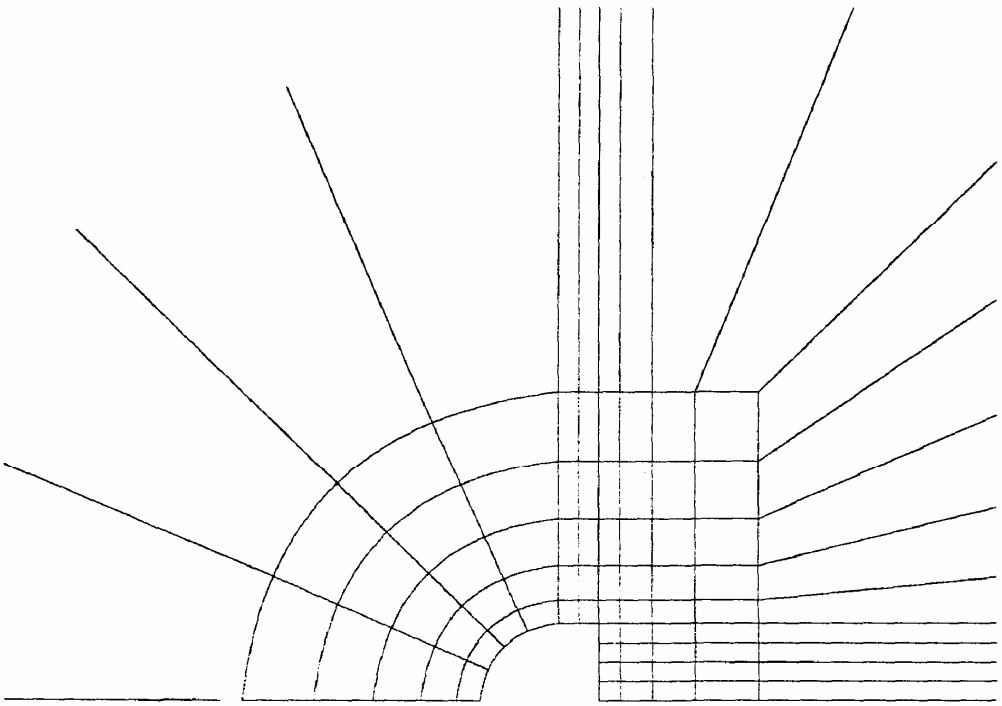

Fig. 7.7

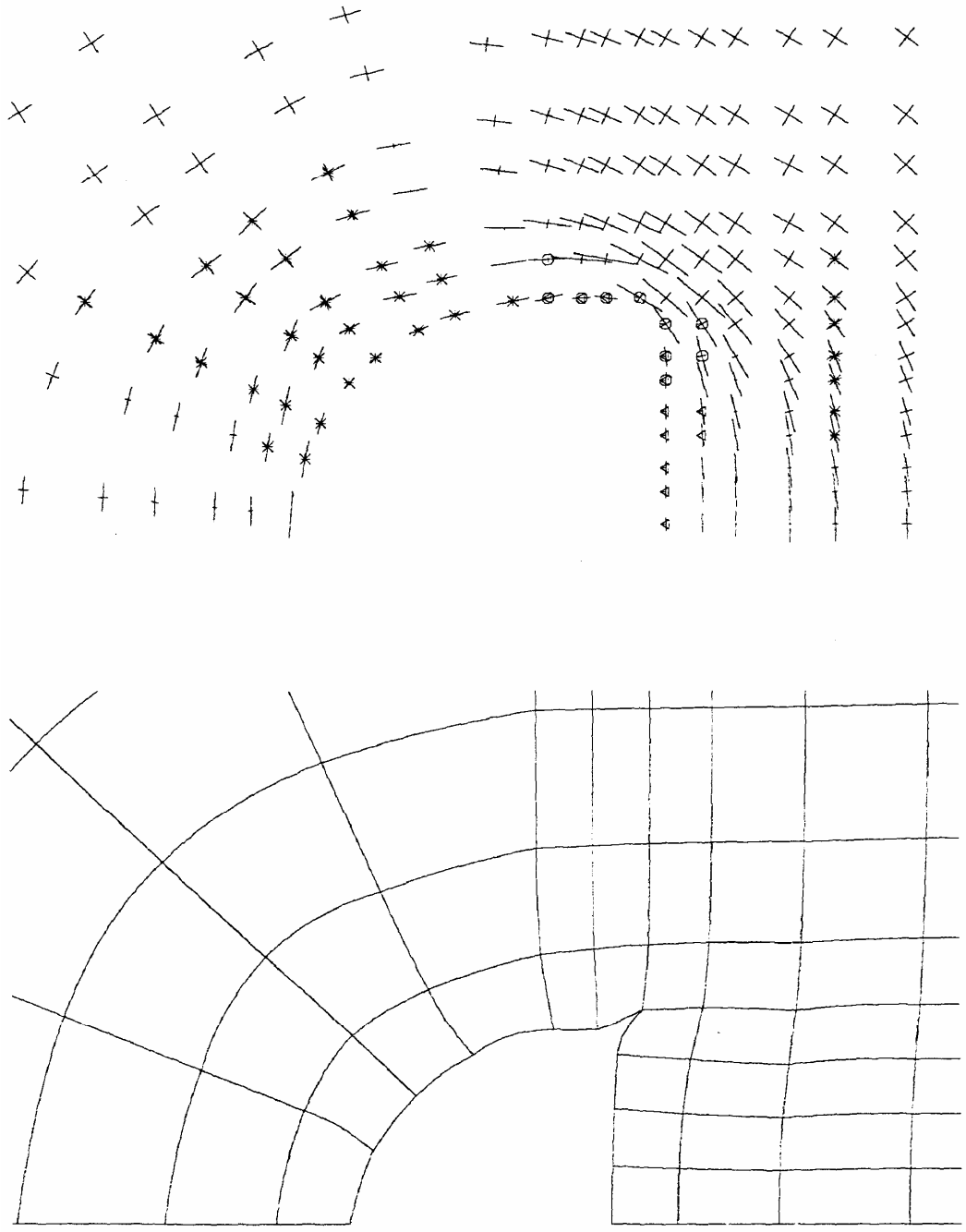

Fig. 7.8

CHAPTER 8. CONCLUSIONS

This report has described the nonlinear finite element program **FESTER.** It is based on the theory of elasto-viscoplasticity, with full provision for using the implicit algorithm, and has a number of distinctive features particularly suited to mining applications, namely:

(i) mapped infinite elements;
(ii) modelling of in situ stress field, and excavation loading;
(iii) one-dimensional joint element;
(iv) small-tension rock model;
(v) modelling of a plane of weakness in the rock, with orthotropic elasticity;
(vi) Modr-Coulomb yield surface;
(vii) account taken of large displacements.

Other features are believed to be new developments, such as:

(viii) use of the Hoek-Brown yield criterion in 3D stress space;
(ix) a Drucker-Prager-type plastic potential with these yield surfaces;
(x) brittle plastic rock model.

A more comprehensive programme of testing the effects of the above features on a set of standard problems should now be undertaken, as well as the program's application to practical mining situations.

ACKNOWLEDGEMENTS

The Authors are grateful to the S.E.R.C. and British Coal for funding the research project, to Professor K.W. Morton (Oxford) and Professor J.R. Whiteman (Brunel) for accommodating the project in their Departments, and to Dr. J.R. Ockendon and Professor S. McKee (co-Investigators).

REFERENCES

Burd, H.J. (1986) Displacement finite element analysis of a reinforced unpaved road. D. Phil, thesis, Oxford University.

Chen, W.F. and Saleeb, A.F. (1982) Constitutive equations for engineering materials, vol.1 - elasticity and modelling. Wiley, New York.

Cormeau, I. (1975) Numerical stability in quasistatic elasto-visco-plasticity. Int. J. Num. Methods Engng. 9, 109-127.

Cramer, H. and Wunderlich, W. (1981) Numerical treatment of rock-structure interaction problems with combined material laws. In: Numerical Methods for Coupled Problems, E. Hinton, P. Bettess and R.W. Lewis eds, Pineridge Press, Swansea, (pp.578-590).

Desai, C.S., Zaman, M.M., Lightner, J.G. and Sriwardane, H.J. (1984). Thin-layer element for interfaces and joints. Int. J. Numer. Anal. Methods Geomech., 8, 19-43.

Dyer, M., Jameiolkowski, M. and Lancellotta, R. (1986) Experimental soil engineering and models for geomechanics. In: Numerical Models in Geomechanics, G.N. Pande and W.F. Van Impe eds, M. Jackson, Redruth, (pp.873-906).

Ghaboussi, E.L., Wilson, E.L. and Isenberg, J. (1973) Finite element for rock joints and interfaces. J. Soil Mech. and Found. Div. ASCE, 99, 833 et seq.

Gibbs, N.E., Poole, W.G. and Stockmeyer, P.K. (1976) An algorithm for reducing the profile and bandwidth of a sparse matrix. SIAM J. Numer. Anal., 13, 236-250.

Goodman, R.E., Taylor, R.L. and Brekke, T.L. (1968) A model for the mechanics of jointed rock. J. Soil Mech. and Found. Div. ASCE, 94, 637-659.

Greenough, C. and Robinson, K. (1981) Finite element library: Level 1 documentation. SERC/Rutherford Appleton Laboratory, Chilton.

Hinton, E. and Owen, D.R.J. (1977) Finite element programming: Academic Press, London.

Hoek, E. (1983) Strength of jointed rock masses. Geotechnique 33, 187-223.

Hoek, E. and Brown, E.T. (1980) Underground excavations in rock. Inst. Mining & Metallurgy, London.

Holt, J.S. and Parsons, B. (1979) Special problems in incremental finite element plasticity analysis. In: The Mathematics of Finite Elements and Applications III, J.R. Whiteman ed., Academic Press, London (pp.415-422).

Hoskins, E.R. (1969) The failure of thick-walled hollow cylinders of isotropic rock. Int. J. Rock Mech. Min. Sci., 6, 99-125.

Kim, M.K. and Lade, P.V. (1984) Modelling rock strength in three dimensions. Int. J. Rock Mech. Min. Sci., 21, 21-33.

Koiter, W.T. (1953) Stress-strain relations, uniqueness and variational theorems for elastic-plastic materials with singular yield surface. Quart. Appl. Math., 11, 350-354.

Korneev, V.G. and Langer, U. (984) Approximate solution of plastic flow theory problems. Teubner, Leipzig.

Marques, J.M.M.C. and Owen, D.R.J. (1984) Infinite elements in quasi-static materially nonlinear problems. Computers and Struct., 18, 739-751.

Naylor, D.J. (1977) Finepak (Mark 2): User instructions and explanatory notes. Univ. College Swansea Dept. Civil Engng report CR/85/76.

Owen, D.R.J. and Hinton, E. (1980) Finite elements in plasticity. Pineridge Press, Swansea.

Pan, X.-D. and Hudson, J.A. (1988) A simplified three-dimensional Hoek-Brown yield criterion. In: Rock Mechanics and Power Plants, M. Romana ed., Madrid (pp.95-104).

Pande, G.N. and Sharma, K.G. (1979). On joint/interface elements and associated problems of numerical ill-conditioning. Int. J. Numer. Anal. Methods Geomech., 3, 293-300.

Prévost, J.H. and Höeg, K. (1975) Soil mechanics and plasticity analysis of strain softening. Géotechnigue, 25, 279-297.

Reed, M.B. (1986a) Numerical solutions for the axisymmetric tunnel problem using the Hoek-Brown criterion. In: Numerical Models in Geomechanics, G.N. Pande and W.F. Van Impe eds, M. Jackson, Redruth (pp.369-374).

Reed, M.B. (1986b) Stresses and displacements around a cylindrical cavity in soft rock. I.M.A. J. Appl. Math., 36, 223-245.

Reed, M.B. (1988a) An elastoviscoplastic model for soft rock. Eng. Comput., 5, 65-70.

Reed, M.B. (1988b) Non-associated flow rules in computational plasticity. In: Numerical Methods in Geomechanics, Innsbruck 1988, G. Swoboda ed., A.A. Balkema, Rotterdam (pp.481-488).

Schaefer, H. (1975) A contribution to the solution of contact problems with the aid of bond elements. Comp. Meths. Appl. Mech. Engng., 6, 335-354.

Schofield, A. and Wroth, P. (1968) Critical state soil mechanics. McGraw-Hill, London.

Sloan, S.W. (1986) An algorithm for profile and wave front reduction of sparse matrices. Int. J. Numer. Meth. Engng., 23, 239-251.

Sloan, S.W. and Randolph, M.F. (1983) Automatic element reordering for finite element analysis with frontal solution schemes. Int. J. Numer. Meth. Engng., 19, 1153-1181.

Sloan, S.W. and Booker, J.R. (1986) Removal of singularities in Tresca and Mohr-Coulomb yield functions. Comm. Appl. Numer. Methods, 2, 173-179.

Stricklin, J.A., Haisler, W. and Reisemann, W. (1973) Evaluation of solution procedures of material and/or geometrically non-linear structural analysis. AIAA J., 11, 292-299.

Thomas, J.N. (1984) An improved accelerated initial stress procedure for elasto-plastic finite element analyses. Int. J. Numer. Anal. Methods Geomech., 8, 359-379.

Zienkiewicz, O.C. (1977) The Finite Element Method, 3rd ed. McGraw-Hill,. London.

Zienkiewicz, O.C. and Pande, G.N. (1977) Time-dependent multilaminate model of rocks -a numerical study of deformation and failure of rock masses. Int. J. Numer. Anal. Methods Geomech., 1, 219-248.